Journal of Colloid and Interface Science 599 (2021) 453–466

Contents lists available at ScienceDirect

Journal of Colloid and Interface Science

journal homepage: www.elsevier.com/locate/jcis

Regular Article

Deposition of zinc cobaltite nanoparticles onto bismuth vanadate for enhanced photoelectrochemical water splitting

Sutripto Majumder [a,*], Nguyen Duc Quang [a], Nguyen Manh Hung [a,b], Nguyen Duc Chinh [a], Chunjoong Kim [a,*], Dojin Kim [a,*]

[a] Department of Materials Science and Engineering, Chungnam National University, Daejeon 34134, Republic of Korea
[b] Department of Materials Science and Engineering, Le Quy Don Technical University, Hanoi, 100000, Viet Nam

HIGHLIGHTS

- $ZnCo_2O_4$ nanoparticles designed to decorate $BiVO_4$ nanoworms to form *n-p* heterojunction.
- Impressive 4.4 fold increase in the photocurrent density was achieved for composite.
- Incorporation of $ZnCo_2O_4$ accelerates the interfacial kinetics of $BiVO_4$.
- Establish correlation between PEC and band structure analysis of the photoelectrodes.
- Understanding the surface kinetics of different photoelectrodes was developed.

GRAPHICAL ABSTRACT

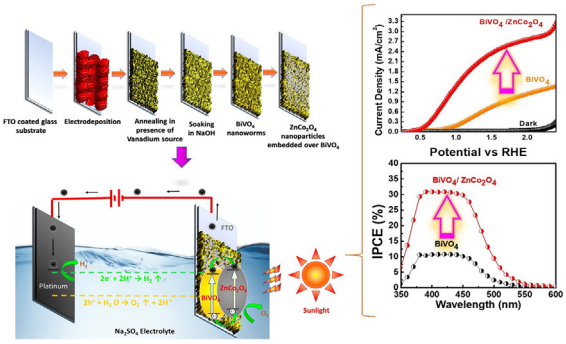

ARTICLE INFO

Article history:
Received 24 November 2020
Revised 1 April 2021
Accepted 22 April 2021
Available online 26 April 2021

Keywords:
Photoelectrochemical
$BiVO_4/ZnCo_2O_4$
$ZnCo_2O_4$
Heterojunction
Water splitting

ABSTRACT

During the past few decades, photoelectrochemical (PEC) water splitting has attracted significant attention because of the reduced production cost of hydrogen obtained by utilizing solar energy. Significant efforts have been invested by the scientific community to produce stable ternary metal oxide semiconductors, which can enhance the stability and increase the overall production of oxygen. Herein, we present the ternary metal oxide deposition of $ZnCo_2O_4$ as a route to obtain a novel photocatalyst layer on $BiVO_4$ to form $BiVO_4/ZnCo_2O_4$ a novel composite photoanode for PEC water splitting. The structural, topographical, and optical analyses were performed using field emission scanning electron microscopy, X-ray diffraction, high-resolution transmission electron microscopy, and UV–Vis spectroscopy to confirm the structure of the $ZnCo_2O_4$ grafted over $BiVO_4$. A remarkable 4.4-fold enhancement of the photocurrent was observed for the $BiVO_4/ZnCo_2O_4$ composite compared with bare $BiVO_4$ under visible illumination. The optimum loading of $ZnCo_2O_4$ over $BiVO_4$ yields unprecedented stable photocurrent density with an apparent cathodic shift of 0.46 V under 1.5 AM simulated light illumination. This is also evidenced by the flat-band potential change through Mott–Schottky analysis, which reveals the formation of *p*-$ZnCo_2O_4$ on *n*-$BiVO_4$. The improvement in the PEC performance of the composite with respect to bare $BiVO_4$ is ascribed to the formation of thin passivating layer of *p*-$ZnCo_2O_4$ on *n*-$BiVO_4$ which improves the kinetics of interfacial charge transfer. Based on our study, we have gained an in-depth understanding of the $BiVO_4/ZnCo_2O_4$ composite as high potential in efficient PEC water splitting devices.

* Corresponding author.
E-mail addresses: sutriptomajumdervnit2013@gmail.com, smajumder_83@cnu.ac.kr (S. Majumder), ckim0218@cnu.ac.kr (C. Kim), dojin@cnu.ac.kr (D. Kim).

https://doi.org/10.1016/j.jcis.2021.04.116
0021-9797/

1. Introduction

The growing global population is driving an ever-increasing demand for energy. Therefore, switching to renewable sources has become necessary. From this perspective, Fujishima and Honda in 1972 introduced an efficient process to convert solar energy to clean chemical energy [1]. Soon after, photoelectrochemical (PEC) water splitting was investigated as a potential method for the conversion of solar energy to fuels such as hydrogen and oxygen. To achieve PEC water splitting, a number of semiconductor materials have been developed and investigated. Semiconductors with the following properties show good response with respect to PEC water splitting: (i) chemical and electrochemical stability in water under illumination, (ii) appropriate band gap, (iii) rapid separation and transfer of electron–hole pairs, (iv) catalytic activity for oxygen/hydrogen evolution reaction, and (v) low fabrication cost [2,3]. Considering the above, multifarious metal oxide semiconductors such as TiO_2, In_2O_3, SnO_2, ZnO, WO_3, Fe_2O_3, and $BiVO_4$ have been extensively studied [4–10]. Among these materials, $BiVO_4$ is considered the most promising material. $BiVO_4$ exhibits a direct optical band gap of 2.3–2.5 eV making it attuned to absorb photons with wavelengths (λ) below 510–560 nm [11]. The position of valance band edge of $BiVO_4$ lies just below the water oxidation level whereas the position of the conduction band (CB) edge is favorably located at 0 V vs. NHE at pH = 0, makes $BiVO_4$ thermodynamically capable of oxygen evolution [12].

Besides possessing good optical absorption properties, $BiVO_4$ also shows to a short-hole diffusion length of ~70 nm which results in poor electron transport [13]**.** This property leads to an increase in the rate of recombination of the photogenerated species, which has a direct impact on the kinetics of the water splitting reaction. Significant efforts have been devoted to overcome the above-mentioned drawbacks by several approaches: (a) manipulation of hierarchical nanostructures [14] (b) doping by foreign elements [15], (c) oxygen evolution co-catalyst loading (OEC) [10,16] and (d) constructing heterojunctions with another semiconductor [17,18]. The method of constructing heterojunctions with other semiconductors has been demonstrated as an effective approach to control the kinetic processes, thereby enhancing the PEC activity of bare $BiVO_4$. The high performance of these heterojunctions is due to the facile charge transport that takes place via the built-in field. Several reports have shown that binary metal oxides such as SnO_2, WO_3, Fe_2O_3, MoO_3, Cu_2O, and Co_3O_4 [19–24] can be used to construct heterojunctions with $BiVO_4$. Among these, multivalent Co-based oxides exhibit highly improved PEC oxidation properties. In addition to the ability of forming heterojunctions, Co-based metal oxides are well-known as good photocatalysts because they can function as rapid transporters for charge carriers by reducing the reaction barrier [25]. Therefore, developing an exceptional Co-based metal-oxide-oriented material for fabricating heterojunctions with $BiVO_4$ is of paramount importance.

Recently, researchers have focused on bimetallic transition oxides, especially $ZnCo_2O_4$, in the field of super capacitors, lithium-ion batteries, gas-sensors, biosensing, catalytic CO oxidation, catalytic CO_2 reduction, and photocatalytic hydrogen evolution [26–32]. Spinel-type $ZnCo_2O_4$ is a readily available, non-hazardous p-type material that possesses a low optical band gap (~2.3–2.5 eV) [33,34]. Compared to individual component oxides of Zn and Co, nanostructured $ZnCo_2O_4$ exhibits the richest redox chemistry with high electrochemical surface areas toward certain reactions [35,36]. This rich chemistry occurs because of the extraordinary structure of $ZnCo_2O_4$, which includes tetrahedral and octahedral voids where Zn^{2+} replaces the Co^{2+} and Co^{3+} that occupy the tetrahedral and octahedral positions, respectively [37]. These voids within the structure are responsible for higher electrical conduction with high PEC stability. Chen *et al.* reported that the valence band (VB) of $ZnCo_2O_4$ comprises the O 2p level, while the conduction band (CB) is composed of the Co 3d-e_g and Co 3d-$t2_g$ levels, which help reduce the rate of recombination of the photogenerated charge carriers intrinsically [38]. Considering the above features, we employed $ZnCo_2O_4$ to create a heterojunction with $BiVO_4$ as an underlying structure to enhance the PEC oxidation of water.

In this study, we grafted $ZnCo_2O_4$ nanoparticles on a $BiVO_4$ nanoworm structure on fluorine-doped tin oxide (FTO) through a simple method. The nanoworm structure was preferred for $BiVO_4$ because this porous structure increases the probability of hole diffusion and light absorption. The formation of *n*-$BiVO_4$/*p*-$ZnCo_2O_4$ was confirmed by structural, morphological, and optical characterizations. The experimental results showed that the optimized $BiVO_4$/$ZnCo_2O_4$ had an exceptionally high photocurrent density as well as superior stability compared to bare $BiVO_4$ in a neutral electrolyte under light irradiation. Herein, we investigate properties such as facile charge transport, which accounts for the high PEC performance, and electron lifetime by various PEC characterizations such as Mott–Schottky (M−S) analysis, electrochemical impedance spectroscopy (EIS), and open-circuit voltage decay (OCVD) measurements. The possible photocatalytic mechanisms are also discussed.

2. Experimental methods

2.1. Preparation of $BiVO_4$ nanoworm structure

A two-step process was adopted for the preparation of the $BiVO_4$ nanoworm structure on the FTO-coated glass substrate. First, a bismuth oxyiodide (BiOI) nanoflake structure was grown by electrodeposition, as discussed in a previous study [39]. Following the same procedure, 0.04 M of $Bi(NO_3)_3$ was mixed with 0.4 M KI to form the plating solution, and the pH of the solution was maintained at ~1.7 by introducing drops of concentrated 2 M HNO_3. The solution was stirred for 30 min, during which a 0.23 M solution of p-benzoquinone was added to the above solution, whereupon the solution became dark olive in color. Cathodic deposition at 145 mV vs. the saturated calomel electrode (SCE) was conducted to form a basic BiOI nanoflake structure on FTO. Transformation of BiOI nanoflakes into the $BiVO_4$ nanoworms was achieved by immersing the as-prepared BiOI nanoflake structure into a solution of vanadyl acetate in dimethyl sulfoxide, followed by slow calcination to 450 °C at a heating rate of 2 °C s^{-1}. After cooling, the samples were soaked in 1 M NaOH solution for 30 min. A bright yellow thin film was obtained, which indicated the formation of $BiVO_4$.

2.2. Preparation of $ZnCo_2O_4$ nanoparticles

Hydrothermal synthesis was conducted to prepare $ZnCo_2O_4$ nanoparticles. Zinc nitrate (1 mM) and cobalt nitrate (2 mM) were added to 40 mL of deionized (DI) water. To ensure the uniform distribution of each component, the mixture was mechanically agitated for 45 min. Liquid ammonia was introduced in the above solution dropwise until the pH of the solution reached 11, and the mixture was stirred for another 20 min. Subsequently, the as-prepared solution was transferred into a 100 mL Teflon-lined stainless-steel autoclave. The autoclave was maintained at 120 °C for 12 h. The resulting precipitates were collected by centrifugation at 5000 rpm and washed with DI water three times. The precipitates were subsequently dried overnight at 80 °C for 12 h. The formation of the $ZnCo_2O_4$ nanoparticles was subsequently confirmed. In addition to $ZnCo_2O_4$ nanoparticles, Co_3O_4, $Zn_{0.25}Co_2O_4$, $Zn_{0.50}Co_2O_4$, and $Zn_{0.75}Co_2O_4$ nanoparticles were also prepared for com-

parison following the above hydrothermal method under the same conditions by altering the molar concentration of the Zn source (i.e. 0.25, 0.50, and 0.75 mM also) with a fixed 2 mM Co source.

2.3. Fabrication of $BiVO_4/ZnCo_2O_4$ electrodes

$ZnCo_2O_4$ nanoparticles (~1 mg) were dispersed in 1 mL absolute ethanol and ultrasonicated for 45 min to form a uniform nanoparticle ink. Subsequently, 20 μL of the $ZnCo_2O_4$ nanoparticle ink was drop-cast onto the $BiVO_4$ electrodes within an area of 2.5 cm^2, which was confirmed by Kapton tapping to form $BiVO_4/ZnCo_2O_4$. Finally, the composite electrode was calcined to 450 °C in air for 1 h at a rate of 1 °C min^{-1}. Furthermore, $BiVO_4/ZnCo_2O_4$ nanocomposite electrodes using different quantities of the dispersed $ZnCo_2O_4$ nanoparticle ink (5, 10, 15, and 25 μL) were prepared (see Fig. 1). For comparison, $BiVO_4$ electrodes were coated with ZnO and Co_3O_4 following the same experimental procedure.

2.4. Material characterization

The structural and phase formation of $BiVO_4$ and $BiVO_4/ZnCo_2O_4$ on the FTO-coated glass substrate as well as FTO was determined using a Rigaku D/MAX-RC diffractometer with Cu Kα radiation (1.541 Å). The surface morphology and elemental compositions of the fabricated photoanodes were monitored by field emission scanning electron microscopy (FE-SEM, JSM700F, JEOL) coupled with energy-dispersive X-ray (EDX) spectroscopy. To investigate the chemical composition of both samples, X-ray photoelectron spectroscopy (XPS, Kratos AXIS Ultra DLD) using an Al-monochromatic Kα X-ray source (hν = 1486.6 eV) was performed, and the work functions of the samples were determined by ultraviolet photoelectron spectroscopy (UPS) using a Thermo Fisher Scientific ESCALAB 250 XI system. The deconvolution of the XPS profiles was carried out using the XPS PEAK41 software package. The optical absorption spectra of the $BiVO_4$ and $BiVO_4/ZnCo_2O_4$ samples on the FTO substrate were characterized using a UV–Vis spectrophotometer (Shimadzu UV-3600) in the range 300–600 nm. Photoluminescence (PL) measurements were carried out using a LabRAM HR-80 instrument in the range 350–900 nm.

2.5. PEC measurements

The PEC water splitting measurements for the fabricated samples were performed using a standard three-electrode system (PGSTAT128N, Metrohm Autolab Instrument). KCl-saturated calomel (Hg/Hg_2Cl_2) also termed as saturated calomel electrode (SCE) served as the reference electrode (RE), Pt as the counter electrode (CE), and the fabricated photoanode was employed as a working electrode (WE). The simulated illumination source was a Xe 150 W lamp with AM 1.5 G, and the light intensity was calibrated to 100 mW cm^{-2} using a Si photodiode. The photoactive area for the fabricated photoanodes was fixed at 0.5 cm^2. The linear sweep voltammograms (LSVs) were obtained in the voltage window of − 0.5 V to 1.7 V vs SCE at a scan rate of 20 mV s^{-1}. An aqueous 0.5 M Na_2SO_4 solution was used as the electrolyte with and without a hole scavenger (0.5 M Na_2SO_3). The incident photon-current conversion efficiency (IPCE) of all electrodes was measured through the chopped monochromator with a 150 W Xe lamp as the simulated light source (designed by HS Technologies, Korea) in the range of 300–700 nm excitation wavelengths at 0.5 V. The IPCE for the samples was determined at the constant potential 1.23 V vs. RHE in a 0.5 M Na_2SO_4 electrolyte using the same three-electrode setup described above for photocurrent measurements. M–S measurements were performed in the dark in the range between − 0.5 V and 1.7 V vs. SCE and a constant frequency of 1 kHz. PEC impedance spectroscopy was conducted under simulated AM 1.5 illumination (100 mW cm^{-2}) in a 0.5 M Na_2SO_4 solution at 0.65 V vs. SCE, by applying a single 10 mV sinusoidal perturbation of the amplitude in the frequency range 10^{-2}–10^5 Hz. The results acquired with the Nova program were fitted in terms of the equivalent circuits with Z-View software. The potential was measured against SCE throughout the experiments and converted to specific values vs. RHE using the following Nernst equation:

$$E(vsRHE) = E(vsSCE) + 0.242V + 0.059 \cdot pH \quad (1)$$

3. Results and discussion

3.1. Structural and morphological properties of the photoelectrodes

The crystal structures of the bare $BiVO_4$ and $BiVO_4/ZnCo_2O_4$ photoelectrodes were investigated using X-ray diffraction (XRD). The XRD patterns of the different samples are shown in Fig. 2 (a). Curve (i) shows the FTO peaks, whereas curves (ii) and (iii) display the peaks of $BiVO_4$ and $BiVO_4/ZnCo_2O_4$, respectively. The peaks denoted by the symbol (♣) within curves (ii) and (iii) were indexed to monoclinic $BiVO_4$ (JCPDS No. 14-0688). Additional peaks observed in pattern (iii), designated by the symbol (♥), were identified as the cubic spinel structure of $ZnCo_2O_4$ (JCPDS No. 23-1390). This confirms the deposition of $ZnCo_2O_4$ on $BiVO_4$. All the samples have a strong background of FTO, indicated by the symbol (*). The formation of $ZnCo_2O_4$ nanoparticles is evidenced by the XRD pattern shown in Fig. S1†. Fig. S1† further confirms that as the concentration of Zn increases from 0.25 to 1 mM (with a constant concentration of Co), the (1 1 1) peak emerges. The XRD pattern for $ZnCo_2O_4$ at a Zn:Co molar ratio of 1:2 confirms the formation of $ZnCo_2O_4$, as it clearly exhibits the formation of the cubic spinel

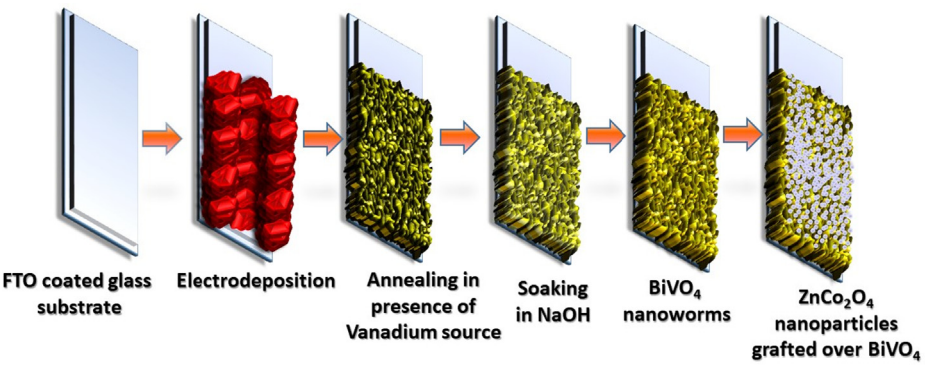

Fig. 1. Schematic of the stepwise fabrication of $BiVO_4/ZnCo_2O_4$ nanostructure photoanode.

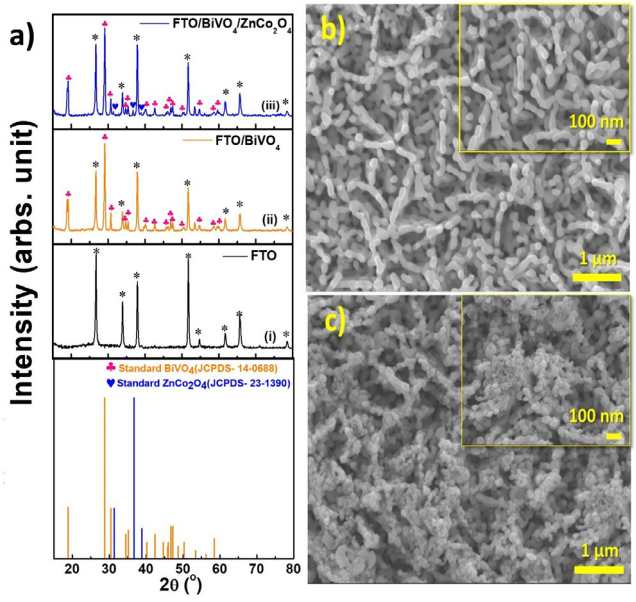

Fig. 2. XRD patterns of (i) FTO, (ii) $BiVO_4$, and (iii) $BiVO_4/ZnCo_2O_4$ photoanodes, (b) and (c) shows the FESEM images of $BiVO_4$ and $BiVO_4/ZnCo_2O_4$ photoanodes at 1 μm and 100 nm (inset).

structure of $ZnCo_2O_4$ with an orientation toward the (3 1 1) plane. Apart from the formation of $ZnCo_2O_4$, Co_3O_4 was also synthesized, as confirmed by JCPDS No. 43-1003. These results are similar to those reported by Cheng *et al.* [40]. Moreover, compared to pure $ZnCo_2O_4$, the XRD pattern of $BiVO_4/ZnCo_2O_4$ shows very few peaks corresponding to $ZnCo_2O_4$, which can be explained by its small loading amount or high dispersion on the $BiVO_4$ nanoworm structure [41].

FE-SEM was employed to investigate the different photoelectrodes. Fig. 2 (b) and (c) show the top-view of the different electrodes at 1 μm scale, showing the conformal growth of the $BiVO_4$ nanoworms on FTO. Similarly Fig. 2 (c) at the same scale shows the uniform deposition of $ZnCo_2O_4$ over $BiVO_4$. The inset of Fig. 2 (b) and 2 (c) displays the zoomed area selected at the 100 nm scale for both the samples. The grafting of $ZnCo_2O_4$ on the $BiVO_4$ nanoworm-like structure was also confirmed by energy-dispersive spectroscopy (EDS), as shown in Fig. S2†. This type of nanoparticle morphology can influence the PEC water splitting properties of metal oxide pristine semiconductors.

The high-resolution transmission electron microscopy (HRTEM) image of $BiVO_4$/ $ZnCo_2O_4$ is shown in Fig. 3. Fig. 3 (a) shows the deposition of the $ZnCo_2O_4$ nanoparticle structure at the edges of the $BiVO_4$ nanoworms. At high resolution (Fig. 3 (b)), the interplanar spacing of 0.243 nm was identified as the (3 1 1) plane of $ZnCo_2O_4$ at the edge of the $BiVO_4$ nanoworm. The presence of $BiVO_4$ was confirmed by the appearance of an interplanar spacing of 0.197 nm, which was identified as the (1 3 2) plane of monoclinic $BiVO_4$. The composition was further investigated by EDS mapping, as shown in Fig. 3 (d)–(h), which confirm the presence of Bi, V, O, Zn, and Co. The formation of an amorphous phase with a crystalline phase at the boundaries is also observed in the TEM images. These interlinked crystalline and amorphous phases can accelerate the charge transfer between active sites because of the flexibility of the local framework in the amorphous phases [42]. Further indication of the formation of $ZnCo_2O_4$ nanoparticles is provided in Fig. S3(a)†. Fig. S3(b)† displays the d-spacing of $ZnCo_2O_4$ nanoparticles, which is in agreement with JCPDS No. 23–1390. The elemental mapping shown in Fig. S3 (d–f)† also confirms the presence of Zn,

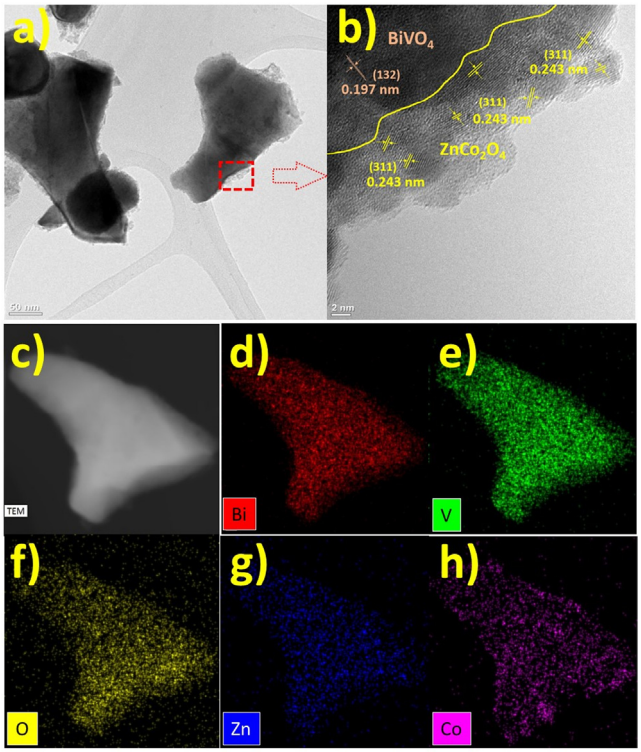

Fig. 3. HRTEM image of $BiVO_4/ZnCo_2O_4$ photoanodes shown at (a) 50 nm (b) 2 nm, (c) TEM image and corresponding elemental mappings of (d) Bi, (e) V, (f) O, (g) Zn, and (h) Co.

Co, and O. The formation of the $ZnCo_2O_4$ nanoparticles is also evidenced in Fig. S3 (g) †.

3.2. Elemental properties of the photoelectrodes

The valence states of both $BiVO_4$ and $BiVO_4/ZnCo_2O_4$ electrodes were characterized by XPS. Comparative XPS profiles (Fig. 4 (a)) showed the characteristic peaks of Bi, O, and V. Additional XPS signals of Zn and Co were found only in the pattern of $BiVO_4/ZnCo_2O_4$. This supports the deposition of $ZnCo_2O_4$ on the $BiVO_4$ nanoworms. In both XPS profiles, adventitious carbonaceous residues were observed on the materials handled in air. Fig. 4 (b)–(f) show the core spectra of Bi, V, O, Zn, and Co, respectively, in $BiVO_4/ZnFe_2O_4$. The Bi 4*f* core-level spectrum is shown in Fig. 4 (b). Binding energy values at 158.5 eV and 163.8 eV correspond to Bi $4f_{7/2}$ and Bi $4f_{5/2}$. Fig. 4 (c) shows the V 2*p* spectrum; the two peaks found at 516.4 eV and 523.9 eV are attributed to V $2p_{3/2}$ and V $2p_{1/2}$, respectively. The deconvolution of O 1*s* shown in Fig. 4 (d) results in peaks positioned at 529.7 eV and 531.2 eV, which can be assigned to oxygen species at the lattice O_L and hydroxyl groups bonded to the metal cations in the oxygen-deficient region O_D, respectively [43,44]. Fig. 4 (e) shows two major deconvoluted peaks at 1021.5 eV and 1044.3 eV ascribed to Zn $2p_{3/2}$ and Zn $2p_{1/2}$ respectively [45]. The Co 2*p* spectrum shown in Fig. 4 (f) is composed of two main peaks at approximately 781 eV and 796 eV, which show a spin orbit splitting of 16 eV between $2p_{3/2}$ and $2p_{1/2}$. Traces of satellite peaks designated as (sat) were observed at 787.4 eV and 804.8 eV; these are typical features of cobalt oxides [46]. After the deconvolution of the basic peaks of $2p_{3/2}$ and $2p_{1/2}$ the coexistence of two different oxidation states Co^{3+} (≈780.5 eV, 795.4 eV) and Co^{2+} (≈781.8 eV, 797.8 eV) was discovered.

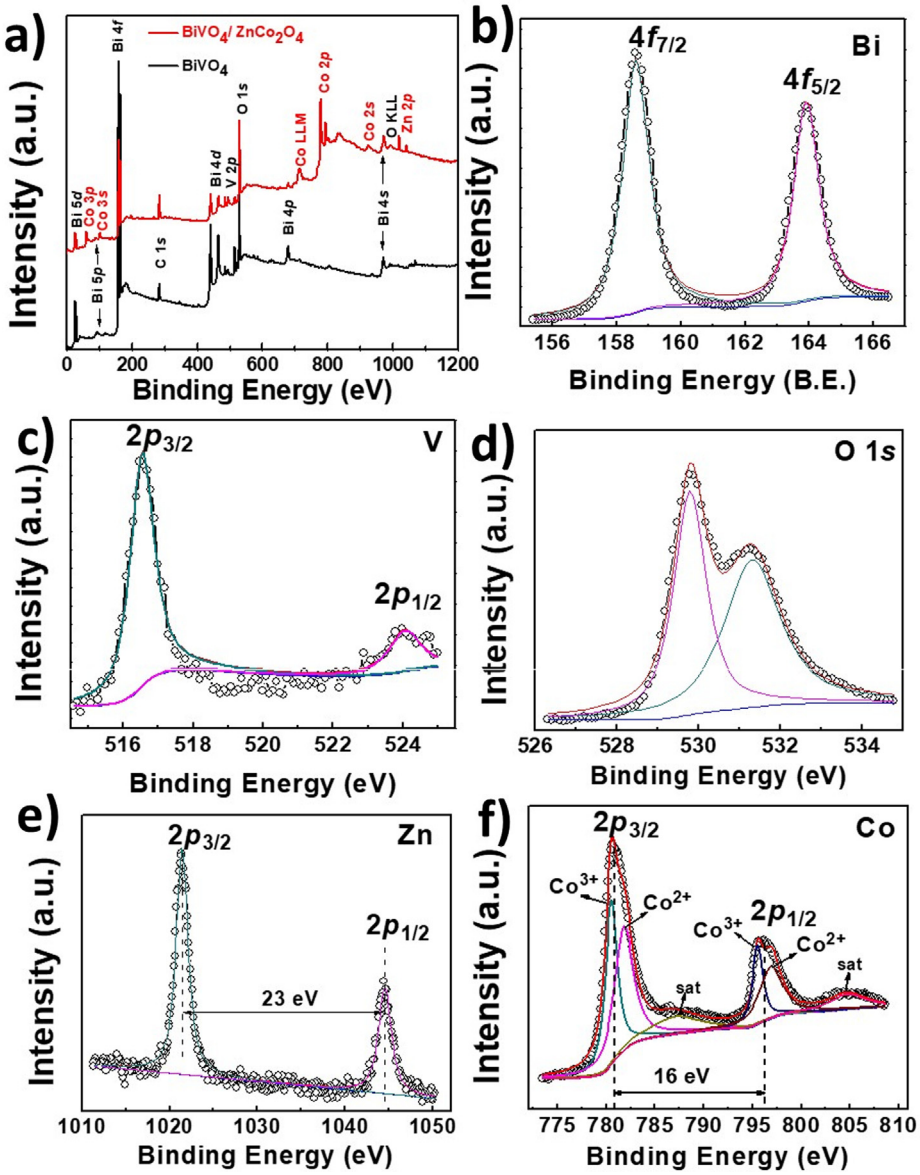

Fig. 4. (a) Overall XPS profiles of $BiVO_4$ and $BiVO_4/ZnCo_2O_4$ and the core levels of (b) Bi 4*f*, (c) V 2*p*, (d) O 1*s*, (e) Zn 2*p*, and (f) Co 2*p* in the $BiVO_4/ZnCo_2O_4$ photoanode.

3.3. Optical properties of the photoelectrodes

Fig. 5 (a) shows the UV–Vis absorption spectra, which reveal that the light absorption edge of $BiVO_4/ZnCo_2O_4$ is similar to that of the bare $BiVO_4$ nanoworm-structured thin film, implying that there is no additional band gap transition caused by the incorporation of $ZnCo_2O_4$ nanoparticles. However, in the same spectra, the light absorption intensity of $BiVO_4/ZnCo_2O_4$ was found to be higher than that of the bare $BiVO_4$ sample, which demonstrates the light-trapping capability of $ZnCo_2O_4$ nanoparticles [47,48].

The optical energy band gap was estimated by Tauc's equation, as shown in the Supporting Information, considering a value of n = 2 for the condition of direct allowed transition. Because of the similar light absorption edges of bare $BiVO_4$ and $BiVO_4/ZnCo_2O_4$, the electrodes possess nearly the same band gap values, as shown in Fig. S4†. The estimated band gaps are 2.47 eV and 2.49 eV for $BiVO_4$ and $BiVO_4/ZnCo_2O_4$, respectively, showing no significant differences.

Relative Photoluminescence (PL) spectra were measured for both samples. The excitation energy were used for this measurement was 320 nm for both the samples. Fig. 5 (b) shows that the PL intensity decreases sharply after grafting the $ZnCo_2O_4$ nanoparticles on the $BiVO_4$ nanoworm structure. This sharp decrease in the PL intensity inhibits radiative recombination of the photogenerated charge carriers, resulting in the separation of electron–hole pairs. This improvement can be attributed to the appropriate alignment of the CB and VB of $BiVO_4$ and $ZnCo_2O_4$.

3.4. PEC properties of the photoelectrodes

The PEC water splitting activity was determined using the three-electrode system described in the experimental section. Fig. 6 (a) shows the LSVs for bare $BiVO_4$ and $BiVO_4/ZnCo_2O_4$. Front-side illumination have been preferred for all the photoelectrodes. The photocurrent densities of bare $BiVO_4$ were measured as 0.43 and 0.89 $mA{\cdot}cm^{-2}$ at 1.23 and 1.6 V (vs RHE), respectively, and increased to 1.92 and 2.62 $mA{\cdot}cm^{-2}$ at 1.23 and 1.6 V vs. RHE, respectively, for the $BiVO_4/ZnCo_2O_4$ photoanode. The increase in the photocurrent density of $BiVO_4/ZnCo_2O_4$ at 1.6 V vs. RHE is approximately 2.94 times higher than that of the bare $BiVO_4$ nano-

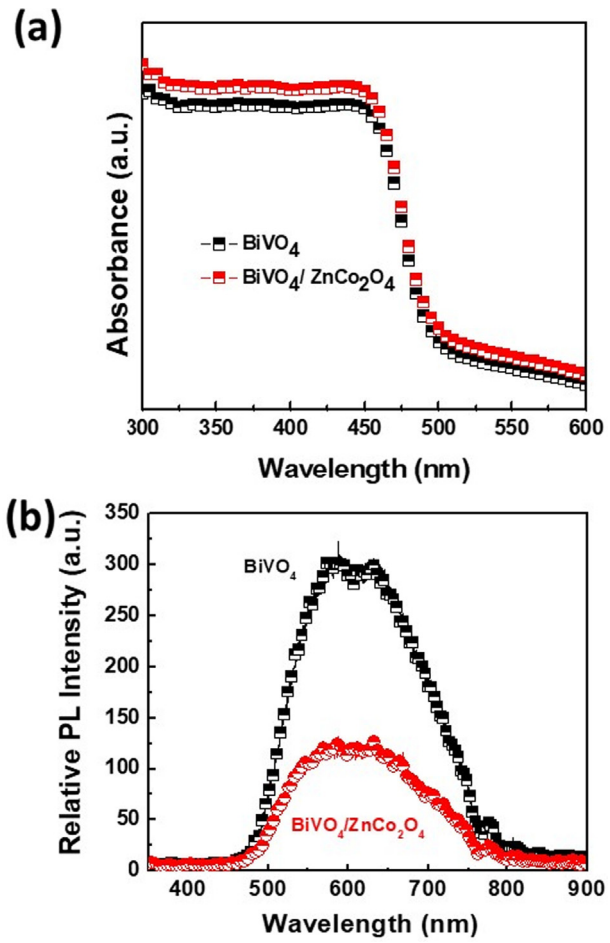

Fig. 5. (a) UV–vis absorption spectra of $BiVO_4$ and $BiVO_4/ZnCo_2O_4$, (b) Relative Photoluminescence spectra of $BiVO_4$ and $BiVO_4/ZnCo_2O_4$.

worm electrode. This increase signifies the extraction of the photoholes from $BiVO_4$ to $ZnCo_2O_4$ [49]. In addition, a distinct negative shift in the onset potential of the $BiVO_4/ZnCo_2O_4$ photoanode compared with the pristine $BiVO_4$ was observed by extrapolating the linear part of the Butler plot (i.e., $(J^2$-V) characteristics), as shown in Fig. S5†. The onset values were estimated as 1.09 and 0.63 V vs. RHE for bare $BiVO_4$ and $BiVO_4/ZnCo_2O_4$, respectively. Under illumination conditions, the incorporation of $ZnCo_2O_4$ on $BiVO_4$ led to an improvement in current densities over the entire operating range from 0.5 V to 2.4 V vs. RHE. Prior to fixing the volume of $ZnCo_2O_4$ as 20 μL, complete optimization of the loading of $ZnCo_2O_4$ nanoparticles was performed, as shown in Fig. S6†. Among the different loading volumes (i.e. 5, 10, 15, 20, and 25 μL), the 20 μL $ZnCo_2O_4$ nanoparticle solution showed the highest photocurrent densities with a comparatively low onset potential through Butler's plot, as shown in Fig. S7†.

In addition to the formation of a uniform interface between $BiVO_4$ and $ZnCo_2O_4$, other composite structures, such as $BiVO_4/Co_3O_4$, $BiVO_4/Zn_{0.25}Co_2O_4$, $BiVO_4/Zn_{0.50}Co_2O_4$, and $BiVO_4/Zn_{0.75}Co_2O_4$ electrodes were also fabricated to characterize their PEC water splitting properties. The experimental conditions for this characterization were the same: AM 1.5 G simulated light with an intensity of 100 $mW{\cdot}cm^{-2}$ in a 0.5 M Na_2SO_4 electrolyte. Fig. S8† shows the response of the different electrodes. From the graph, it is clear that the coating of $ZnCo_2O_4$ at the Zn:Co ratio of 1:2 responded the best in terms of water oxidation. Photocurrent densities for $BiVO_4$, $BiVO_4/Co_3O_4$, $BiVO_4/Zn_{0.25}Co_2O_4$, $BiVO_4/Zn_{0.50}Co_2O_4$, $BiVO_4/Zn_{0.75}Co_2O_4$, and $BiVO_4/ZnCo_2O_4$ photoelectrodes, were mentioned in the (Table T1†). To determine the onset potential, the linear part of the Butler plot (i.e., J-V characteristics) was extrapolated, as shown in Fig. S9†. The onset potential values were shown in the (Table T1†) for different electrodes, respectively, indicating a gradual shift toward lower potentials.

Fig. 6(a) shows the periodic chronoamperometric photocurrent results for $BiVO_4$ and $BiVO_4/ZnCo_2O_4$. The recorded values are consistent with the values obtained from the LSVs. Both photoanodes exhibited an immediate rise in the photocurrent under irradiation and a rapid quenching to zero when the light is removed. The $BiVO_4/ZnCo_2O_4$ photoanode showed the maximum increase to 2.4–2.7 $mA{\cdot}cm^{-2}$ vs RHE, which is approximately 2.9 times higher than that of pristine $BiVO_4$ (0.89–0.7 $mA{\cdot}cm^{-2}$ vs RHE). Furthermore, the applied bias photoconversion efficiencies for both samples were calculated based on the J-V curve as a function of the applied voltage, as shown in Fig. 6 (b). Further evaluation of the photoactivity was conducted using the applied bias photon-to-current efficiency (ABPCE), which was calculated from the Eq. (S2) in the Supporting Information for both samples. Considering about the different pitfalls described [50,51]. Therefore we have found JV characteristics of $BiVO_4$ and $BiVO_4/ZnCo_2O_4$ as a two terminal device shown in the Fig. S10†. The $BiVO_4/ZnCo_2O_4$ photoanode showed the highest ABPCE of approximately 0.07% at 0.86 V vs RHE, while the pristine $BiVO_4$ photoanode showed an ABPCE of 0.03% at 0.89 V vs RHE. The clear evidence of the high value of the ABPCE were found for $ZnCo_2O_4$ on $BiVO_4$ nanoworms photoelectrode than bare $BiVO_4$ which is due to fast separation of photoexcited electrons and holes. Fig. 6 (c) shows the photocurrent density–time (I–t) curve of both electrodes at 1.23 V vs. RHE. After grafting, a substantial improvement over pristine $BiVO_4$ in the photostability was recorded for 3 h of continuous PEC water splitting, as shown in Fig. 6 (d). The bare $BiVO_4$ nanowire structure possesses a higher chemical and photocorrosion response than the $BiVO_4/ZnCo_2O_4$ composite structure. Quantitatively, $BiVO_4/ZnCo_2O_4$ retains 97% of its initial photocurrent density, while bare $BiVO_4$ retains approximately 70% after 3 h of photoexposure. The bare $BiVO_4$ in photoelectrochemically unstable due to the dissolution of V and Bi which as suggested by Zhang *et al.* [52]. Other than this Yao *et al.* reported that $BiVO_4$ go through the preferential dissolution of Vanadium in to the products such as V_2O_5, V_3O_5 and VO_2 in comparison with Bismuth [53]. For better understanding of the above facts we have perform chronoamperometric for 24 h of exposure under standard illumination condition shown in Fig. S11†. EDS have been carried out as the post-mortem analysis of both the samples before and after chronoamperometric stability test for 24 h of standard light exposure shown as Fig. S12†. Form Fig. S12 (a) †, S12 (b) † shows before and after 24 h of standard light exposure it is found that the basic $BiVO_4$ started degrading heavily after 20 h resulting in the breakdown of the sample this is due to the high degradation rate of V and Bi (discussed earlier). Again form the Fig. S12 (c) † $BiVO_4/ZnCo_2O_4$ it is clear that the weight % of both Zn and Co is relatively lower after 24 h of long stability condition. As suggested earlier this degradation may happen due to the basic dissolution of the V and Bi within the $BiVO_4$ which acts as the base layer. Thus it is clear that due to the formation of the proper heterojunction between $BiVO_4$ and $ZnCo_2O_4$, acts as a protective layer over $BiVO_4$ as a result of which relatively less degradation have been observed which is also understood from the Fig. S12 (c) † and S12 (d) †. However variation in the content of weight % for both Zn and Co through EDS for the $BiVO_4/ZnCo_2O_4$ samples after 24 h have also been evidenced.

The external quantum efficiencies (EQEs) of the $BiVO_4$ nanoworms and $BiVO_4/ZnCo_2O_4$ samples were measured to determine the influence of $ZnCo_2O_4$ on $BiVO_4$. Fig. 7(a) shows the EQE photoresponse of $BiVO_4$ and $BiVO_4/ZnCo_2O_4$ over the range 350–600 nm. Again, from the response of $BiVO_4$ and $BiVO_4/ZnCo_2O_4$ shown in the Fig. 7 (a) is quiet similar to the work presented over

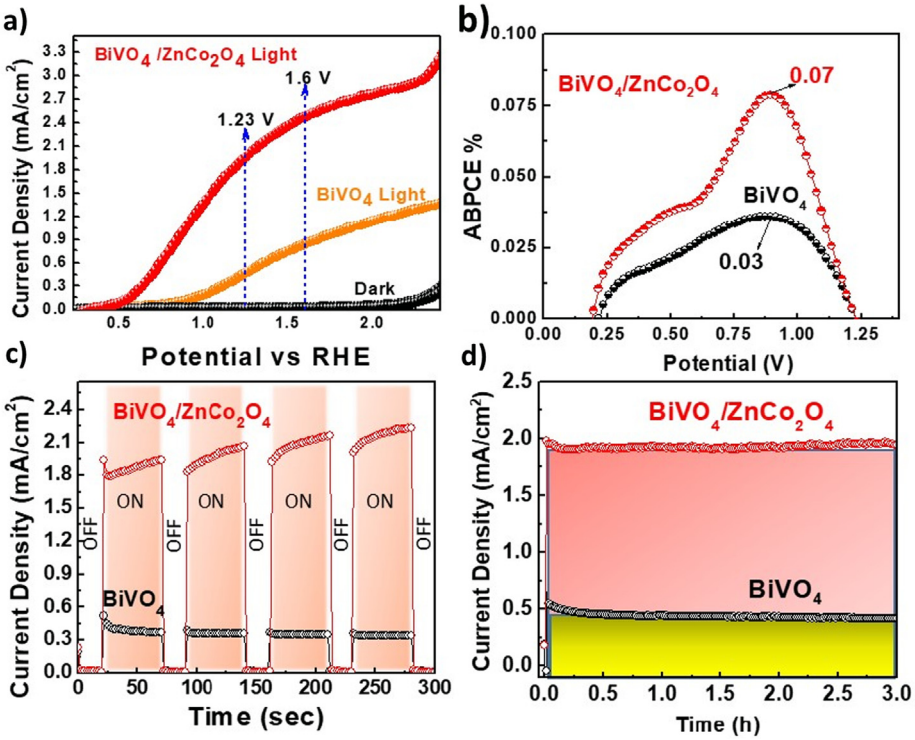

Fig. 6. (a) LSVs of $BiVO_4$ and $BiVO_4/ZnCo_2O_4$ photoanodes measured with and without 1.5 G illumination (100 $mW.cm^{-1}$), (b) applied bias photon-to-current efficiencies (ABPCE) of the photoanodes under AM 1.5 G (100 $mW.cm^{-2}$) illumination, (c) transient photocurrents of the different photoanodes, (d) stability test for the respective electrodes. The data were collected considering a 0.5 M Na_2SO_4 electrolyte at pH = 7.

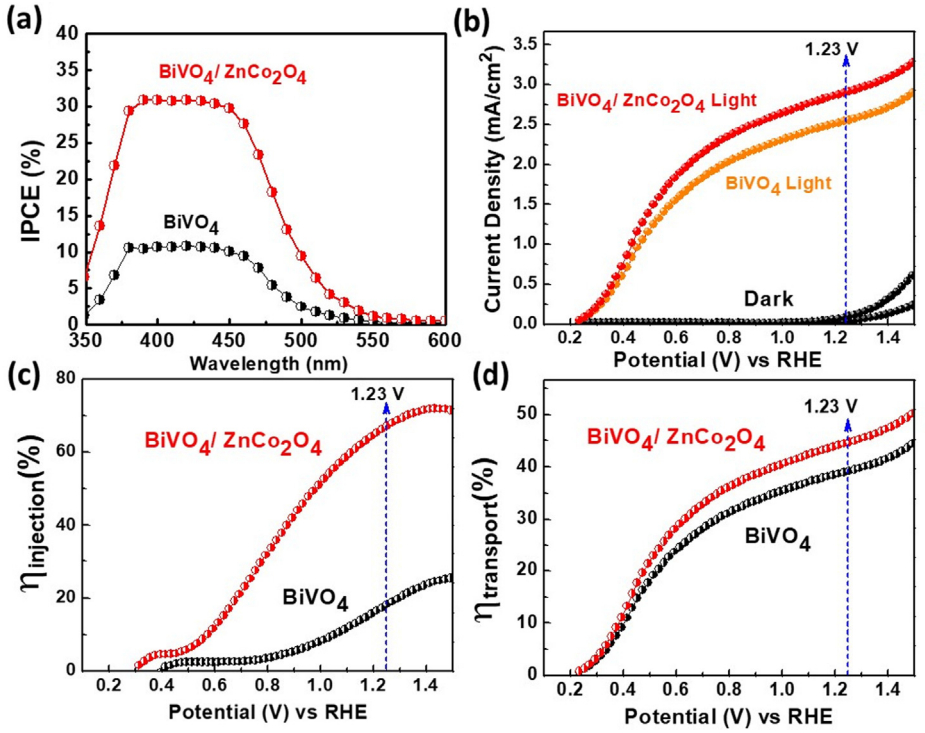

Fig. 7. (a) Incident photon-to-current conversion spectra of $BiVO_4$ and $BiVO_4/ZnCo_2O_4$ electrodes, (b) LSVs of pristine $BiVO_4$ and $BiVO_4/ZnCo_2O_4$ in 0.5 M Na_2SO_4 + Na_2SO_3 electrolyte, (c) calculated charge transport efficiency, and (d) charge injection efficiency of $BiVO_4$ and $BiVO_4/ZnCo_2O_4$ nanostructured thin films.

$BiVO_4$ based photoelectrodes in the different reports [54–56]. The IPCE of $BiVO_4/ ZnCo_2O_4$ is higher than that of bare $BiVO_4$. The IPCE values of $BiVO_4/ ZnCo_2O_4$ and bare $BiVO_4$ at 400 nm are approximately 30.3% and 10.08%, respectively, which indicates an approximately 2.73-fold increase. The factors that affect the IPCE are partial absorption of the incident photons and electron–hole

recombination before their collection [57]. However, the dominating factors that can improve the IPCE values of the photoelectrode depend on the light harvesting efficiency (LHE), charge injection, and separation efficiencies [58]. The LHE as estimated from the equation S6 described in the Supporting Information shows the values for both the samples are shown in Fig. S13†. The relatively high IPCE of the $BiVO_4/ZnCo_2O_4$ sample can be attributed to the enhanced light absorption, which accelerates charge transfer compared to the bare $BiVO_4$ nanoworm structure.

Further, for the quantification of the charge separation and injection effect caused by the decoration of $ZnCo_2O_4$ on the $BiVO_4$ nanoworm structure, the charge separation efficiency ($\eta_{seperation}$) and surface charge injection efficiency ($\eta_{injection}$) were investigated [59]. For this, a sacrificial reagent (0.5 M Na_2SO_3) was injected into the previously used 0.5 M Na_2SO_4 electrolyte. This sacrificial agent is considered to provide 100% of the surface catalytic efficiency that is caused by kinetically faster reactions with the reagent anions with respect to the kinetically controlled oxygen evolution reaction [60]. $\eta_{separation}$ is defined as the amount of photogenerated holes reaching the electrode/electrolyte interface, which can be estimated by the ratio of photocurrent density measured with the 0.5 M Na_2SO_3 electrolyte to the photoabsorption rate. The LSVs of $BiVO_4$ and $BiVO_4/ZnCo_2O_4$ with Na_2SO_3 were measured at the same scan rate under AM 1.5 G illumination. Fig. 7(b) displays different reaction kinetics with the addition of the Na_2SO_3 scavenger into the neutral Na_2SO_4 electrolyte for both photoanodes. The photocurrent densities were 2.54 and 2.89 $mA{\cdot}cm^{-2}$ at 1.23 V vs RHE for $BiVO_4$ and $BiVO_4/ZnCo_2O_4$, respectively.

The above results indicate that the composite $BiVO_4/ZnCo_2O_4$ exhibits more efficient charge transport and charge injection properties than those of bare $BiVO_4$. Prior to the estimation of the separation and injection efficiencies, the values of the integrated photocurrent (J_{abs}) of $BiVO_4$ and $BiVO_4/ZnCo_2O_4$ photoanodes were calculated from Figures S14† and S15† as 5.93 and 6.06 $mA{\cdot}cm^{-2}$, respectively. According to the LSV shown in Fig. 7(c), the $\eta_{separation}$ of the $BiVO_4/ZnCo_2O_4$ photoanode increases with increasing applied potential as arises from the equation S7 described in the Supporting Information. The $\eta_{separation}$ value of $BiVO_4$ was 38.47%, while that of $BiVO_4/ZnCo_2O_4$ was 44.63% at 1.23 V vs. RHE. The high value of $\eta_{separation}$ for $BiVO_4/ZnCo_2O_4$ is due to the structural porosity at the nanoscale and the formation of good heterogeneity [61–63]. Similar trends have been reported by Abdi *et al.* where p-n junctions have been used to enhance the charge separation and photo voltage provided by $BiVO_4$ photoanodes [64].

On the other hand, the injection efficiency depends on the amount of photogenerated holes reaching the surface during electrochemical reactions, which can be estimated by the ratio of photocurrent densities measured with and without the hole scavenger (Na_2SO_3 electrolyte). A large potential gap in the entire range, as shown in the LSV in Fig. 7(d), indicates the low value of $\eta_{injection}$ for bare $BiVO_4$ compared to that of $BiVO_4/ZnCo_2O_4$. Further, the above facts become clear from Fig. 7 (d), which quantitatively arises from the equation S8 described in the Supporting Information. The $\eta_{injection}$ for $BiVO_4/ZnCo_2O_4$ was approximately 68.17%, which is significantly higher than the 18.24% measured for the bare $BiVO_4$ nanoworm at 1.23 V vs. RHE. The high value of $\eta_{injection}$ for $BiVO_4/ZnCo_2O_4$ suggests that the coating of $ZnCo_2O_4$ on $BiVO_4$ decreases the surface recombination of the photogenerated holes, which increases the kinetics of oxygen evolution at the surface. Dotan *et al.* reported that surface trap states are closely related to $\eta_{injection}$ [65]. The inferior $\eta_{injection}$ values of bare $BiVO_4$ are attributed to a high number of surface traps at the electrode/electrolyte interface, which results in low surface reaction and high surface recombination. Furthermore, as from the HRTEM it is clear that presence of both crystalline and the amorphous phases of $ZnCo_2O_4$ in which the behavior of amorphous phase may acts as a coating of a catalyst which disabled the action of surface traps at the electrode/electrolyte interface when anodic potential is applied. Along with this the catalytic nature of pristine $ZnCo_2O_4$ can be evidenced from the Fig. S16†. The high value of $\eta_{injection}$ for the $BiVO_4/ZnCo_2O_4$ samples has a positive impact not only on the photocurrent density, but also on the value of the cathodic onset potential shift with respect to bare $BiVO_4$.

The electrochemical flat-band potentials (E_{fb}) of $BiVO_4$ and $BiVO_4/ZnCo_2O_4$ were measured using M−S plots based on the equation S9 in the Supporting Information [66]. The intercept plotted between the capacitance (vertical axis) and the voltage (horizontal axis), as shown in Fig. 8 (a), determines the value of E_{fb} in the presence of the 0.5 M Na_2SO_4 electrolyte. The $BiVO_4/ZnCo_2O_4$ composite sample shows a negative shift in E_{fb} with respect to the bare $BiVO_4$ nanoworm structure. This behavior implies that the $BiVO_4/ZnCo_2O_4$ sample possesses better band bending, which enhances the charge separation within the interface, as suggested by Wang *et al.* [67]. Moreover, this negative shift in the E_{fb} of $BiVO_4/ZnCo_2O_4$ is accompanied by the accelerated interfacial charge transfer of the photoanode, which suggests a more rapid charge transfer during water oxidation [68]. The donor density (N_d) values were estimated from Fig. 8 (a). The values of N_d were calculated using the formula in the Supporting Information S10. For the bare $BiVO_4$ nanoworm structure, the value of N_d was 3.21×10^{16} cm^{-3}, whereas for the $BiVO_4/ZnCo_2O_4$ sample, it was 10.5×10^{16} cm^{-3} (Table T2†). The high N_d values indicate the high accumulation of charge carriers, which directly promotes the charge transport property of the electrodes. Along with $BiVO_4$ and its composite with $ZnCo_2O_4$, M−S analysis was also carried out for bare $ZnCo_2O_4$, as shown in Fig. S17†. The negative slope with an E_{fb} of 0.26 V indicates that $ZnCo_2O_4$ is a *p*-type structure.

To understand the interfacial properties for all photoanodes, electrochemical impedance spectroscopy (EIS) was implemented. The EIS measurements were carried out with 0.01 V amplitude perturbation in 0.5 M Na_2SO_4 electrolyte at an applied potential varying from 0.535 to 1.735 V vs RHE under both dark and simulated white light shown in the Fig. S18†. For this data a simple Randles circuit is used with minimum number of RC couple circuit to fit the Nyquist Plots [69] as shown in the Fig. S19†. In the equivalent circuit having the components such as R_s which represents the resistance of the electrolyte, R_{ct} is the charge transfer resistance of PEC water oxidation reaction, and CPE is the constant phase element. Similar equivalent circuit (i.e. R_s, R_{ct} and CPE) were found to demonstrated by the Wang *et al.* for iron-cobalt oxide based photocatalyst coated over $BiVO_4$[70]. The trends of Nyquist Plot for both dark and light were found to be similar for both $BiVO_4$, $BiVO_4/ZnCo_2O_4$ respectively. Also it is clear that at the dark condition for both $BiVO_4$ and $BiVO_4/ZnCo_2O_4$ the Nyquist plot forms as an open arc with different applied potential shown in Fig. S18† (a), S18† (b). As an effect of the illumination the response of the Nyquist plot was found to show semicircular behavior with the different applied potential.

Further explore the influence of $ZnCo_2O_4$ on the charge recombination. Focus have been made over the comparative Nyquist plots (i.e., complex-plane impedance plots) for the illumination condition which are shown in Fig. 8 (b). It is evident that the radius of the semicircle decreases as the basic $BiVO_4$ nanoworm structure is coated with $ZnCo_2O_4$ which shows fast charge transfer between electrodes and electrolyte. From Table T2†, a small difference in the value of R_s is observed. The value of R_{ct} gradually decreases when $BiVO_4$ was coated by $ZnCo_2O_4$, indicating that the coating of $ZnCo_2O_4$ substantially accelerated hole transfer into the surface. The higher value of CPE indicates a higher donor density, which is also confirmed by M−S analysis. Overall, the $ZnCo_2O_4$-layered $BiVO_4$ enhances the water oxidation kinetics by (a) reducing surface

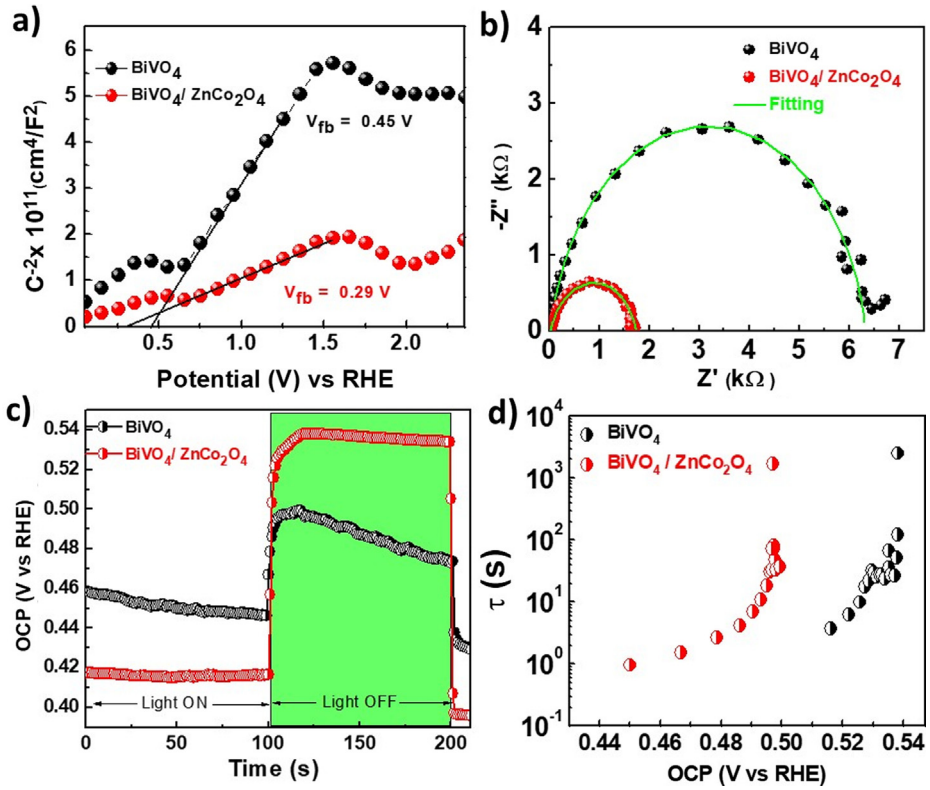

Fig. 8. (a) M–S curves of $BiVO_4$ and $BiVO_4/ZnCo_2O_4$ photoanodes measured in the dark at 1000 Hz, (b) Nyquist Plot of $BiVO_4$ and $BiVO_4/ZnCo_2O_4$ photoanodes measured at 1.23 V vs RHE in 1.5 G illumination (100 mW cm^{-1}). The 0.5 M of Na_2SO_4 with pH 7 were used as an electrolyte, (c) Open-circuit potential photovoltage (V_{oc}) versus time curve measurements in 0.5 M Na_2SO_4 solution for the different photoelectrodes measured with light switched ON and turned OFF for 100 s, (d) Calculated OCP vs lifetime plots for both $BiVO_4$ and $BiVO_4/ZnCo_2O_4$ photoanodes.

recombination, and (b) promoting charge transfer from the surface of $BiVO_4$ to the electrolyte.

From the Fig. S20† (a) and (b) shows R_{ct} and CPE values from the Nyquist plots at different potentials within the range 0.535–1.735 V vs RHE. As the photoexcitation of $BiVO_4$ is obligatory to supply holes to the surface state hence the dark characteristics is different from those of illumination. In the dark the values of the R_{ct} is comparatively large and goes on increasing with the applied potential which further indicates slow water oxidation kinetics from valence band holes [71]. Comparative to the bare $BiVO_4$ the samples coated with $ZnCo_2O_4$ shows relatively lower R_{ct} values. On illumination comparative to the bare $BiVO_4$ the $BiVO_4/ZnCo_2O_4$ samples shows relatively lower R_{ct} values.

The values of the CPE obtained for all samples were found to lie in the range of 10^{-6}-10^{-4} μF shown in the Fig. S16† (b) within the voltage range 0.535–1.735 V vs RHE. It can be found that for both dark and illumination the bare $BiVO_4$ shows one capacitive peak at 0.8 V vs RHE which has been attributed to the V^{4+}/V^{5+} redox couple [72,73]. Further the Trześniewski *et al.* also suggested that the photo charging treatment involving reduction of V^{5+} to V^{4+} they also suggest that this reduction does not affect the bulk electronic properties of the sample [73]. The values of the CPE goes on decreases as there is the increase in the applied potential beyond 1 V vs. RHE. The response of the CPE for $BiVO_4/ZnCo_2O_4$ found to show higher than bare $BiVO_4$ and decreases with the increasing applied potential. The shifting in the response of CPE and R_{ct} under illumination indicates that hole transfer for the water-splitting reaction takes place through the surface states.

Investigation of the enhancement in the PEC activity of $BiVO_4/ZnCo_2O_4$ with respect to the bare $BiVO_4$ nanoworm electrode was analyzed by open-circuit photovoltage (OCP) studies. OCP is measured as the difference between the open-circuit V_{oc} in the dark and V_{oc} at simulated AM 1.5 illumination. Zhong *et al.* suggested that the OCP signifies the degree of band bending as it is the difference between the Fermi level of the photoanode and the CE [74]. Irradiation of the surface of the photoanodes results in charge separation, which generates photoelectrons. This is also indicated by the shifting of the OCP toward a negative value, as shown in Fig. 8 (c). Meanwhile, the photogenerated holes that are collected at the surface of the photoanodes are ready for water oxidation. When the accumulation of photoelectrons reaches saturation, the photovoltage reaches a steady state. The OCP of $BiVO_4$ under illumination is lower than that of $BiVO_4/ZnCo_2O_4$, which originates from the existence of the trap states [75]. The coating of $ZnCo_2O_4$ on $BiVO_4$ shows better a build-up of the OCP, which implies that surface modifications by $ZnCo_2O_4$ passivate the surface states of bare $BiVO_4$ [76]. Moreover, this build-up of OCP values enhances the separation of photocharges at the electrode/electrolyte interface. Under the dark condition, the position of the Fermi level of $BiVO_4/ZnCo_2O_4$ photoanodes with respect to the redox potential of the electrolyte shows a more cathodic nature of the OCP with respect to $BiVO_4$; the accumulated charge carriers increase the transient OCP, which leads to a smaller decay lifetime. The smaller decay lifetime signifies a higher charge transfer efficiency [77]. Therefore, we focus on the decay lifetime, which enables electron–hole separation at the interface. In our experiment, $BiVO_4/ZnCo_2O_4$ samples that show larger band bending as per the M–S equation exhibit higher charge accumulation than $BiVO_4$ samples. The correlation observed between the decay lifetime and the accumulated electrons has been modeled by Bisquert and coworkers, and is given as [78]:

$$\tau = \frac{k_B T}{e}\left[\frac{dOCP}{dt}\right]^{-1} \quad (2)$$

The formula shows that the decay lifetime is inversely proportional to the derivative of the transient decay. Fig. 8 (d) shows the calculated decay lifetime (τ) vs. OCP (V vs. RHE). In general, the values of ΔOCP for $BiVO_4/ZnCo_2O_4$ are higher than those of the bare $BiVO_4$ nanoworm structure. An increase in the value of the OCP directly indicates the presence of an internal electric field. Under the OFF condition, the value of the decay lifetime (τ) for $BiVO_4/ZnCo_2O_4$ was 0.94 s, which was found to be shorter than that of $BiVO_4$, whose value was 3.65 s (Table T2†). The comparatively high decay time for bare $BiVO_4$ with respect to $BiVO_4/ZnCo_2O_4$ suggests the recombination of the accumulated photocharge carriers [79]. A similar trend for τ has been observed by Antony *et al.* [80]. A comparatively lower value of τ for $BiVO_4/ZnCo_2O_4$ indicates that the coating of $ZnCo_2O_4$ enhances the injection efficiency.

As He discharge source (which emits the wavelength of ~58.4 nm that is corresponding to the energy of 21.2 eV in the vacuum ultraviolet region) exhibits very small line width makes UPS as the most sophisticated and powerful tool with very high resolution of the order of (<0.1 eV) help to scrutinize the band positions very accurately [81]. The values of E_f is as depicted were referenced to metal standard. The band edge positions for $BiVO_4$ and $ZnCo_2O_4$ which were grown separately over FTO substrate were plotted with respect to E_{vac} as shown in the Fig. S21†. The left-hand side for all the figures shows a low-binding-energy cut-off region, whereas the right-hand side shows a high-binding-energy region. In order to deduce the exact values of E_L and E_H, we extrapolate the leading edge to the extended baseline, creating an intersection point in both binding energy regions. As shown in Fig. S21†(a)-(c), work function (ϕ) is estimated by the difference in E_H from the excitation energy of He (21.22 eV) as from equation S11. The individual ϕ of FTO, $BiVO_4$ on FTO, and $ZnCo_2O_4$ over FTO were found to be 4.6 eV, 5.70 eV and 3.98 eV respectively.

Other parameters such as E_{VBM} and E_{CBM} were estimated through the equation S12 and S13 shown in the Supporting Information. Along with this Fig. S22† shows the optical studies which displays the band gap values of the $ZnCo_2O_4$ nanoparticles over FTO were around 2.16 eV which is in between the range of the band gap reported earlier [82]. The variation in the band gap values of $ZnCo_2O_4$ lies on the Co 3d orbital which determines the conduction band level of $ZnCo_2O_4$ that introduce two different energy levels (a) unfilled high energy level of Co 3d-e_g and (b) partially filled Co 3d-$t2_g$ orbital situated at the mid band gap [83,84]. Apart from this the value of FTO/$BiVO_4$ were analyzed in Fig. 9 (a). All the values have been listed in the Table T3†.

From Fig. 9 (b), when the *p-n* junction is illuminated, each of the constituents ($ZnCo_2O_4$ and $BiVO_4$) of the composite generates photoinduced charge carriers (electron–hole pairs). The photogenerated electrons in the CB of $ZnCo_2O_4$ can be easily transferred to the CB of $BiVO_4$ owing to the higher CB of $ZnCo_2O_4$ than $BiVO_4$. Subsequently, the photoelectrons in the CB of $BiVO_4$ can rapidly transfer to the cathode (Pt electrode), where they participate in the reduction of water to form H_2. This reduces the rate of photogenerated charge recombination, whereas the distribution of $ZnCo_2O_4$ nanoparticles further increases the charge transport rate. In the meantime, the photogenerated holes start migrating from the VB of $BiVO_4$ to the VB of $ZnCo_2O_4$ to participate in oxidation of water. This leads to enhanced PEC performance of the $BiVO_4/ZnCo_2O_4$ photoanode. The explanation for the band structure depends upon the mechanism which is discussed in the mechanism section.

Furthermore the flat band estimation through the M−S analysis of FTO/$BiVO_4$ as shown in the Fig. 8 (a) shows the positive slope positioned at 0.45 V vs RHE, which clarifies the *n*-type behavior. Also it is expected that the conduction band minima is near to 0.45 V vs RHE. Again, from Fig. S17† M−S plot for FTO/$ZnCo_2O_4$ demonstrates negative slope. Sarkar *et al.* have explained the significance of negative slope which denotes the flat band from the depletion region of the $1/C^2$ plot [85]. Thus the valance band maxima is 0.26 V vs RHE.

Apart from the values estimated by M−S plot the spectroscopic (i.e. UPS) method shows the position of the conduction band maxima of $BiVO_4$ is 5.7 eV vs vacuum whereas the valance band minima of $ZnCo_2O_4$ lies at 4.62 eV vs vacuum. Therefore in order to set the correlation the positions of CBs and VBs of the $BiVO_4$ and $ZnCo_2O_4$ structure relative to the electrochemical potentials E^o (H^+/H_2) and E^o (O_2/H_2O) have been investigated through UPS [86] we have employed 4.44 eV vs vacuum as the reference value for the electrochemical reduction of water 0 V vs RHE [87]. The calculated values as per UPS for the conduction band minima of $BiVO_4$ is 0.52 V vs RHE whereas the valance band maxima of $ZnCo_2O_4$ lies at 0.18 V vs RHE.

The difference or gap between the flat band values and the conduction band minima for $BiVO_4$ is equal to 0.07 V vs RHE which are quiet admissible as the values are within the range of 0.1–0.2 V vs RHE as reported by the Resasco *et al.* [88], on the other hand the gap between the flat band values and the valance band maxima of $ZnCo_2O_4$ is around 0.08 V vs RHE. Similar trend have been reported by Morales-Guio *et al.* for the *p*-type semiconductors [89]. The little discrepancy in the estimation of the values of flat band can be attributed to the different sample environment such as M−S performed in the presence of electrolyte whereas the UPS measured on the surface of the sample in the vacuum condition [90]. Moreover the values for the $BiVO_4$ was 0.45 V vs RHE which found to be similar as that of the reported by Yassin *et al.* [91]whereas the flat band of the composite were found to be decreasing to 0.29 V vs RHE. This decreasing trend in the flat band values when $BiVO_4$ were coated with other *p*-type materials to form composite shows quiet similar as were reported earlier [92].

Now along with the flat band estimation by M−S the photocurrent onset which is relating with the Butler analysis is also an alternative method for determining the flat band potential. This method is based on measurement of the net photocurrent as a function of applied potential. The flat band potential is predicted to be at the intercept of the square of the net photocurrent with the potential axis. The onset potential derived by the Butler equation is given by the following relationship [93]

$$(V - V_{fb}) \propto \left[\frac{J_{photo}}{\alpha w q P_{light}}\right]^2 \quad (3)$$

where α is the optical absorption coefficient which is wavelength dependent, w stands for space charge width, q is the elementary charge and P_{light} is the light intensity [94]. The estimation of onset potential of the electrode is measured through the light to charge energy conversion performance of the photoelectrode [95]. From Eq. (2) the term V_{fb} is designated as the superficial flat band potential which conveys the information about the kinetic over potential (η) and the potential drop across the Helmholtz layer (η_H) [25]. In here, $BiVO_4$ nanoworm structure were fabricated and whose surface area enhanced when $ZnCo_2O_4$ nanoparticles where deposited over this structure. The onset potential for $BiVO_4$ through Butler plot was found around 1.06 V vs RHE this is due to severe Fermi level pinning effect which has been also identified as the low photovoltages. Hermans *et al.* has pointed out that fermi level pinning of bare $BiVO_4$ happens due to the wet chemical synthesis method that leads to the presence of water and other carbonaceous species [96]. Further the incorporation of $ZnCo_2O_4$ over $BiVO_4$ has lower down onset potential to 0.63 V vs RHE which suppress the effect of Fermi level pinning which was also evidenced by Yin *et al.* [97].

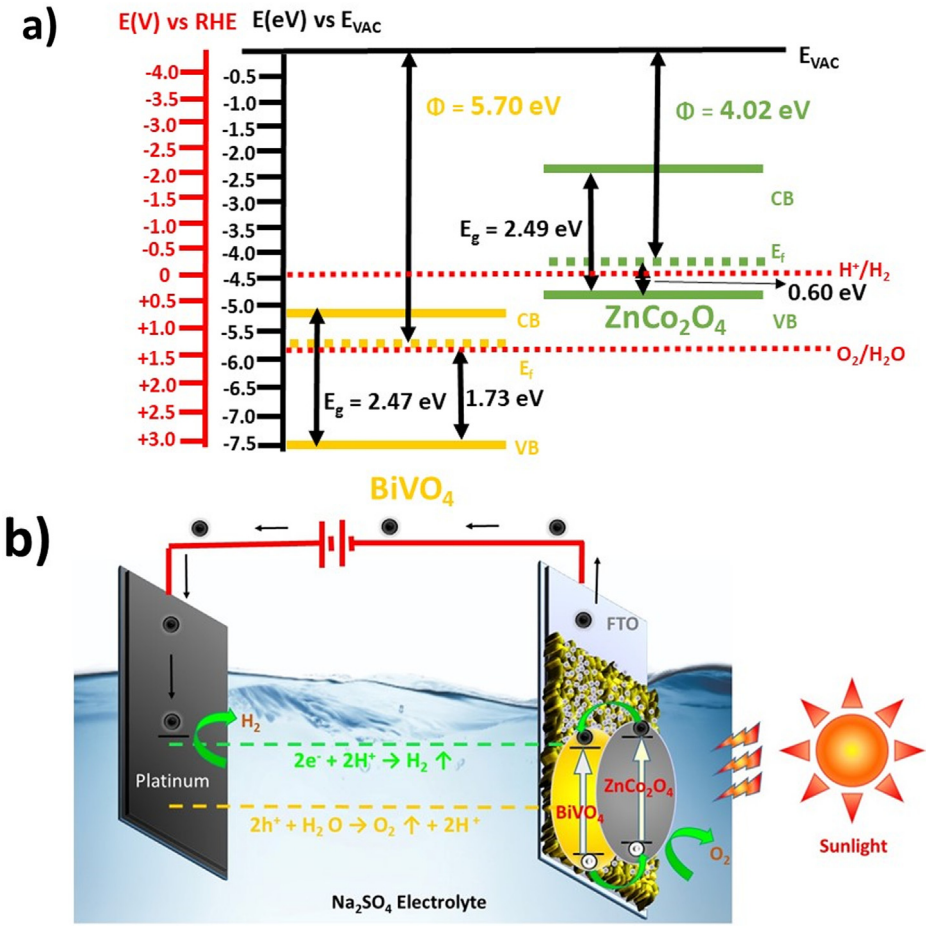

Fig. 9. (a) Estimated Fermi levels of FTO/ $BiVO_4$, and FTO/$ZnCo_2O_4$ with respect to vacuum and RHE scale respectively, (b) schematic of the charge movement based on the vacuum energy level in the pH = 6.5 electrolyte.

3.5. Mechanism

From Fig. 9 it is clear that in general the conduction band and the valance band positions of $ZnCo_2O_4$ is more positive than $BiVO_4$ on the RHE scale. But when the fermi levels align the $BiVO_4$ fermi level will raise little up whilst the $ZnCo_2O_4$ fermi level will low down with respect to relative energy as shown in the Fig. 9 (b). However from M−S it is found that there is the negative shift in the E_{fb} as the $ZnCo_2O_4$ is coated over the $BiVO_4$ nanostructure which directly leads to the higher band bending at the electrode/-electrolyte interface shown in the Fig. S23†. That means the fermi level of the heterostructure $BiVO_4/ZnCo_2O_4$ move far from the position of the vacuum level due to the coating $ZnCo_2O_4$ over $BiVO_4$ structure with respect to the bare $BiVO_4$. Similar trend have been observed by Bai *et al.* at the $BiVO_4/Cu_2O$ heterojunction [23]. Therefore this will inhibit the photo excited electron-hole recombination. Moreover, higher band bending related directly to the surface kinetics by enhancing the surface voltage which is also confirmed by the enhanced OCP of $BiVO_4/ZnCo_2O_4$ heterojunction relative to bare $BiVO_4$. These results are line with the values of CB, E_f and VB level estimated through UPS. Thus the junction which is formed at the interface were found to show staggered type-II heterojunction.

Lastly recalling the discussion of HRTEM images of the $BiVO_4/ZnCo_2O_4$ shows the coexistence of interlinked crystalline and the amorphous phases may acts as a catalyst and it is known that the catalysts acts as the passivating layer for overall enhanced photoelectrochemical response of the structure [98–100]. In the same context it is found that the high values of the injection efficiency rather than separation efficiency also have been reported by the Meng *et al.* were they coated amorphous TiO_2 layer over $BiVO_4$/CuO heterojunction [101]. Therefore the amorphous $ZnCo_2O_4$ may also act as a catalyst for the sluggish OER reaction as it is already none that Cobalt based materials are widely known for being good OER catalyst. As a whole both the improvement in the charge separation and hole selectivity have been observed by the trends of both injection and the separation efficiencies.

The reasons why $BiVO_4/ZnCo_2O_4$ photoanodes show excellent PEC activity are as follows: (i) $BiVO_4/ZnCo_2O_4$ possesses a high surface-to-volume ratio; (ii) the $BiVO_4$ nanoworms anchored with $ZnCo_2O_4$ enhance light absorption; (iii) the optimum coating of $ZnCo_2O_4$ creates an *n-p* heterojunction that generates built-in potential at the heterojunction. As a result, more free charges accumulate at the junction, which is also revealed by the M−S analysis; (iv) As illustrated from HRTEM the amorphous layer of $ZnCo_2O_4$ coated over the pristine $BiVO_4$ structure acts also as a catalyst acts as the which can facilitate charge injection that provides more photogenerated paths, which is crucial for the enhancement of PEC water splitting.

4. Conclusion

We explored a cost-effective approach to develop $ZnCo_2O_4$ nanoparticles as a novel *p*-type material deposited over *n*-$BiVO_4$ to form a type-II staggered *n-p* $BiVO_4/ZnCo_2O_4$ heterojunction for

advanced PEC water splitting. Morphologically, the nanoworm structure of $BiVO_4$ embedded with $ZnCo_2O_4$ nanoparticles creates an optimum layer porosity, which limits the recombination of the photogenerated charge carriers, thereby improving electrolyte penetration which directly enhance a photocurrent density of 1.92 mA·cm^{-2} at 1.23 V vs. RHE, while that of the bare $BiVO_4$ nanoworm structure is approximately 0.43 mA·cm^{-2}. The incorporation of $ZnCo_2O_4$ also form the amorphous phase (as evidenced by HRTEM analysis) which is found to be interlinked with the crystalline phase acts as a well passivating layer which directly enhance the injection efficiency of the structure. Due to the above combined influence of both heterojunction formation and the catalytic nature of $ZnCo_2O_4$ over $BiVO_4$ directly effects the following properties such as (i) change in cathodic shift from 1.09 to 0.63 V vs. RHE, (ii) 2.3-fold improvement in the ABPCE, and (iii) 3-fold increase in the IPCE for the *n-p* BiVO4/$ZnCo_2O_4$ heterojunction with respect to the bare $BiVO_4$ nanoworm structure were achieved. The above findings allow us to gain an in-depth understanding of dual behavior of *p*-$ZnCo_2O_4$ nanoparticles over the *n*-$BiVO_4$ nanowire structure for PEC water splitting by enhanced charge separation and charge injection through efficient hole extraction at the $ZnCo_2O_4$/electrolyte interface. From the performance point of view our vision for future work emphasizes over the exploration of other low cost ternary metal cobaltite as it has a significant potential to enhance photoelectrochemical response for the water splitting.

CRediT authorship contribution statement

Sutripto Majumder: Conceptualization, Methodology, Formal analysis, Data curation, Validation, Writing - original draft, Writing - review & editing. **Nguyen Duc Quang:** Formal analysis, Data curation. **Nguyen Manh Hung:** Formal analysis. **Nguyen Duc Chinh:** Formal analysis. **Chunjoong Kim:** Validation, Formal analysis. **Dojin Kim:** Supervision, Resources, Writing - review & editing.

Declaration of Competing Interest

The authors declare that they have no known competing financial interests or personal relationships that could have appeared to influence the work reported in this paper.

Acknowledgement

This work was supported by the National Research Lab program (2018R1A2A1A05023126) of the National Research Foundation of Korea.

Appendix A. Supplementary material

Supplementary data to this article can be found online at https://doi.org/10.1016/j.jcis.2021.04.116.

References

[1] A. Fujishima, K. Honda, Electrochemical Photolysis of Water at a Semiconductor Electrode, Nature 238 (5358) (1972) 37–38.
[2] D. Cui, L. Wang, K. Xu, L. Ren, L. Wang, Y. Yu, Y. Du, W. Hao, Band-gap engineering of BiOCl with oxygen vacancies for efficient photooxidation properties under visible-light irradiation, J. Mater. Chem. A 6 (5) (2018) 2193–2199.
[3] D. Chen, Z. Liu, Z. Guo, W. Yan, M. Ruan, Decorating Cu2O photocathode with noble-metal-free Al and NiS cocatalysts for efficient photoelectrochemical water splitting by light harvesting management and charge separation design, Chem. Eng. J. 381 (2020) 122655.
[4] A. Miyoshi, S. Nishioka, K. Maeda, Water Splitting on Rutile TiO2-Based Photocatalysts, Chem. – A Eur. J. 24 (69) (2018) 18204–18219.
[5] C. Chen, J. Moir, N. Soheilnia, B. Mahler, L. Hoch, K. Liao, V. Hoepfner, P. O'Brien, C. Qian, L. He, G.A. Ozin, Morphology-controlled In2O3 nanostructures enhance the performance of photoelectrochemical water oxidation, Nanoscale 7 (8) (2015) 3683–3693.
[6] S.-Y. Chen, J.-S. Yang, J.-J. Wu, Three-Dimensional Undoped Crystalline SnO2 Nanodendrite Arrays Enable Efficient Charge Separation in BiVO4/SnO2 Heterojunction Photoanodes for Photoelectrochemical Water Splitting, ACS Appl. Energy Mater. 1 (5) (2018) 2143–2149.
[7] J. Kegel, I.M. Povey, M.E. Pemble, Zinc oxide for solar water splitting: A brief review of the material's challenges and associated opportunities, Nano Energy 54 (2018) 409–428.
[8] A. Jelinska, K. Bienkowski, M. Jadwiszczak, M. Pisarek, M. Strawski, D. Kurzydlowski, R. Solarska, J. Augustynski, Enhanced Photocatalytic Water Splitting on Very Thin WO3 Films Activated by High-Temperature Annealing, ACS Catal. 8 (11) (2018) 10573–10580.
[9] F. Bouhjar, B. Bessaïs, B. Marí, Ultrathin-layer α-Fe2O3 deposited under hematite for solar water splitting, J. Solid State Electrochem. 22 (8) (2018) 2347–2356.
[10] B. Zhang, L. Wang, Y. Zhang, Y. Ding, Y. Bi, Ultrathin FeOOH Nanolayers with Abundant Oxygen Vacancies on BiVO4 Photoanodes for Efficient Water Oxidation, Angew. Chem. 57 (8) (2018) 2248–2252.
[11] H. Huang, L. Liu, Y. Zhang, N. Tian, Novel BiIO4/BiVO4 composite photocatalyst with highly improved visible-light-induced photocatalytic performance for rhodamine B degradation and photocurrent generation, RSC Adv. 5 (2) (2015) 1161–1167.
[12] S. Kohtani, K. Yoshida, T. Maekawa, A. Iwase, A. Kudo, H. Miyabe, R. Nakagaki, Loading effects of silver oxides upon generation of reactive oxygen species in semiconductor photocatalysis, PCCP 10 (20) (2008) 2986–2992.
[13] H.L. Tan, R. Amal, Y.H. Ng, Alternative strategies in improving the photocatalytic and photoelectrochemical activities of visible light-driven BiVO4: a review, J. Mater. Chem. A 5 (32) (2017) 16498–16521.
[14] M. Fang, G. Dong, R. Wei, J.C. Ho, Hierarchical Nanostructures: Design for Sustainable Water Splitting, Adv. Energy Mater. 7 (23) (2017) 1700559.
[15] S.K. Cho, H.S. Park, H.C. Lee, K.M. Nam, A.J. Bard, Metal Doping of BiVO4 by Composite Electrodeposition with Improved Photoelectrochemical Water Oxidation, The Journal of Physical Chemistry C 117 (44) (2013) 23048–23056.
[16] R.-T. Gao, D. He, L. Wu, K. Hu, X. Liu, Y. Su, L. Wang, Towards Long-Term Photostability of Nickel Hydroxide/BiVO4 Photoanodes for Oxygen Evolution Catalysts via In Situ Catalyst Tuning, Angew. Chem. 59 (15) (2020) 6213–6218.
[17] S. Ju, H.-J. Seok, J. Jun, D. Huh, S. Son, K. Kim, W. Kim, S. Baek, H.-K. Kim, H. Lee, Fully blossomed WO3/BiVO4 structure obtained via active facet engineering of patterned FTO for highly efficient Water splitting, Appl. Catal. B 263 (2020) 118362.
[18] Z. Wei, D. Benlin, Z. Fengxia, T. Xinyue, X. Jiming, Z. Lili, L. Shiyin, D.Y.C. Leung, C. Sun, A novel 3D plasmonic p-n heterojunction photocatalyst: Ag nanoparticles on flower-like p-Ag2S/n-BiVO4 and its excellent photocatalytic reduction and oxidation activities, Appl. Catal. B 229 (2018) 171–180.
[19] M. García-Tecedor, D. Cardenas-Morcoso, R. Fernández-Climent, S. Giménez, The Role of Underlayers and Overlayers in Thin Film BiVO4 Photoanodes for Solar Water Splitting, Adv. Mater. Interface 6 (15) (2019) 1900299.
[20] S. Selim, L. Francàs, M. García-Tecedor, S. Corby, C. Blackman, S. Gimenez, J.R. Durrant, A. Kafizas, WO3/BiVO4: impact of charge separation at the timescale of water oxidation, Chem. Sci. 10 (9) (2019) 2643–2652.
[21] Y.-L. Li, Y. Liu, Y.-J. Hao, X.-J. Wang, R.-H. Liu, F.-T. Li, Fabrication of core-shell BiVO4@Fe2O3 heterojunctions for realizing photocatalytic hydrogen evolution via conduction band elevation, Mater. Des. 187 (2020) 108379.
[22] H. He, Y. Zhou, G. Ke, X. Zhong, M. Yang, L. Bian, K. Lv, F. Dong, Improved Surface Charge Transfer in MoO3/BiVO4 Heterojunction Film for Photoelectrochemical Water Oxidation, Electrochim. Acta 257 (2017) 181–191.
[23] S. Bai, J. Liu, M. Cui, R. Luo, J. He, A. Chen, Two-step electrodeposition to fabricate the p–n heterojunction of a Cu2O/BiVO4 photoanode for the enhancement of photoelectrochemical water splitting, Dalton Trans. 47 (19) (2018) 6763–6771.
[24] X. Chang, T. Wang, P. Zhang, J. Zhang, A. Li, J. Gong, Enhanced Surface Reaction Kinetics and Charge Separation of p–n Heterojunction Co3O4/BiVO4 Photoanodes, J. Am. Chem. Soc. 137 (26) (2015) 8356–8359.
[25] S. Chen, D. Huang, P. Xu, W. Xue, L. Lei, M. Cheng, R. Wang, X. Liu, R. Deng, Semiconductor-based photocatalysts for photocatalytic and photoelectrochemical water splitting: will we stop with photocorrosion?, J. Mater. Chem. A 8 (5) (2020) 2286–2322.
[26] L. Xu, Y. Zhao, J. Lian, Y. Xu, J. Bao, J. Qiu, L. Xu, H. Xu, M. Hua, H. Li, Morphology controlled preparation of ZnCo2O4 nanostructures for asymmetric supercapacitor with ultrahigh energy density, Energy 123 (2017) 296–304.
[27] R.A. Adams, V.G. Pol, A. Varma, Tailored Solution Combustion Synthesis of High Performance ZnCo2O4 Anode Materials for Lithium-Ion Batteries, Ind. Eng. Chem. Res. 56 (25) (2017) 7173–7183.
[28] C.R. Mariappan, R. Kumar, G. Vijaya Prakash, Functional properties of ZnCo2O4 nano-particles obtained by thermal decomposition of a solution of binary metal nitrates, RSC Advances 5 (34) (2015) 26843–26849.
[29] C. Shiqiang, L. Li, Y. Ding, J. Zhang, Q. Wu, Z. Hu, Uniform ordered mesoporous ZnCo2O4 nanospheres for super-sensitive enzyme-free H2O2 biosensing and glucose biofuel cell applications, Nano Res. 10 (2017) 2482–2494.
[30] F. Wang, X. Wang, D. Liu, J. Zhen, J. Li, H. Zhang, Investigation of ZnCo2O4–Pt hybrids with different morphologies towards catalytic CO oxidation, Dalton Trans. 44 (48) (2015) 21124–21130.

[31] Y. Bo, C. Gao, Y. Xiong, Recent advances in engineering active sites for photocatalytic CO2 reduction, Nanoscale 12 (23) (2020) 12196–12209.
[32] W. Zhang, C. Xu, E. Liu, J. Fan, X. Hu, Facile strategy to construction Z-scheme ZnCo2O4/g-C3N4 photocatalyst with efficient H2 evolution activity, Appl. Surf. Sci. 515 (2020) 146039.
[33] S. Kim, J.A. Cianfrone, P. Sadik, K.-W. Kim, M. Ivill, D.P. Norton, Room temperature deposited oxide p-n junction using p-type zinc-cobalt-oxide, J. Appl. Phys. 107 (10) (2010) 103538.
[34] Z. Wang, P.K. Nayak, J.A. Caraveo-Frescas, H.N. Alshareef, Recent Developments in p-Type Oxide Semiconductor Materials and Devices, Adv. Mater. 28 (20) (2016) 3831–3892.
[35] B. Subramanian, N. Prakash, K. Thirumalai, M. Muruganandham, M. Sillanpää, M. Swaminathan, Facile Construction of Heterostructured BiVO4–ZnO and Its Dual Application of Greater Solar Photocatalytic Activity and Self-Cleaning Property, Ind. Eng. Chem. Res. 53 (2014) 8346–8356.
[36] J. Wang, F. Osterloh, Limiting factors for photochemical charge separation in BiVO4/Co3O4, a highly active photocatalyst for water oxidation in sunlight, J. Mater. Chem. A 2 (2014).
[37] D. Zhang, Y. Zhang, X. Li, Y. Luo, H. Huang, J. wang, P.K. Chu, Self-assembly of mesoporous ZnCo2O4 nanomaterials: density functional theory calculation and flexible all-solid-state energy storage, J. Mater. Chem. A 4 (2) (2016) 568–577.
[38] J. Chen, J. Zhan, Y. Zhang, Y. Tang, Construction of a novel ZnCo2O4/Bi2O3 heterojunction photocatalyst with enhanced visible light photocatalytic activity, Chin. Chem. Lett. 30 (3) (2019) 735–738.
[39] D. Lee, A. Kvit, K.-S. Choi, Enabling solar water oxidation by BiVO4 photoanodes in basic media, Chem. Mater. 30 (2018) 4704–4712.
[40] J. Cheng, Y. Lu, K. Qiu, H. Yan, X. Hou, J. Xu, L. Han, X. Liu, J.-K. Kim, Y. Luo, Mesoporous ZnCo2O4 nanoflakes grown on nickel foam as electrodes for high performance supercapacitors, PCCP 17 (26) (2015) 17016–17022.
[41] P. Guan, H. Bai, F. Wang, H. Yu, D. Xu, W. Fan, W. Shi, In-situ anchoring Ag through organic polymer for configuring efficient plasmonic BiVO4 photoanode, Chem. Eng. J. 358 (2019) 658–665.
[42] H. Han, H. Choi, S. Mhin, Y.-R. Hong, K.M. Kim, J. Kwon, G. Ali, K.Y. Chung, M. Je, H.N. Umh, D.-H. Lim, K. Davey, S.-Z. Qiao, U. Paik, T. Song, Advantageous crystalline–amorphous phase boundary for enhanced electrochemical water oxidation, Energy Environ. Sci. 12 (8) (2019) 2443–2454.
[43] X. Zhang, J. Qin, Y. Xue, P. Yu, B. Zhang, L. Wang, R. Liu, Effect of aspect ratio and surface defects on the photocatalytic activity of ZnO nanorods, Sci. Rep. 4 (1) (2014) 4596.
[44] P.T. Hsieh, Y.C. Chen, K.S. Kao, C.M. Wang, Luminescence mechanism of ZnO thin film investigated by XPS measurement, Appl. Phys. A 90 (2) (2008) 317–321.
[45] W. Luo, X. Hu, Y. Sun, Y. Huang, Electrospun porous ZnCo2O4 nanotubes as a high-performance anode material for lithium-ion batteries, J. Mater. Chem. 22 (18) (2012) 8916–8921.
[46] R.V. Jagadeesh, H. Junge, M.-M. Pohl, J. Radnik, A. Brückner, M. Beller, Selective Oxidation of Alcohols to Esters Using Heterogeneous Co3O4–N@C Catalysts under Mild Conditions, J. Am. Chem. Soc. 135 (29) (2013) 10776–10782.
[47] J. Wei, C. Zhou, Y. Xin, X. Li, L. Zhao, Z. Liu, Cooperation effect of heterojunction and co-catalyst in BiVO4/Bi2S3/NiOOH photoanode for improving photoelectrochemical performances, New J. Chem. 42 (24) (2018) 19415–19422.
[48] Z.F. Liu, X. Wang, Efficient photoelectrochemical water splitting of CaBi6O10 decorated with Cu2O and NiOOH for improved photogenerated carriers, Int. J. Hydrogen Energy 43 (29) (2018) 13276–13283.
[49] R. Chen, C. Zhen, Y. Yang, X. Sun, J.T.S. Irvine, L. Wang, G. Liu, H.-M. Cheng, Boosting photoelectrochemical water splitting performance of Ta3N5 nanorod array photoanodes by forming a dual co-catalyst shell, Nano Energy 59 (2019) 683–688.
[50] Z. Chen, T.F. Jaramillo, T.G. Deutsch, A. Kleiman-Shwarsctein, A.J. Forman, N. Gaillard, R. Garland, K. Takanabe, C. Heske, M. Sunkara, E.W. McFarland, K. Domen, E.L. Miller, J.A. Turner, H.N. Dinh, Accelerating materials development for photoelectrochemical hydrogen production: Standards for methods, definitions, and reporting protocols, J. Mater. Res. 25 (1) (2010) 3–16.
[51] K. Sivula, R. van de Krol, Semiconducting materials for photoelectrochemical energy conversion, Nat. Rev. Mater. 1 (2) (2016) 15010.
[52] S. Zhang, I. Ahmet, S.-H. Kim, O. Kasian, A.M. Mingers, P. Schnell, M. Kölbach, J. Lim, A. Fischer, K.J.J. Mayrhofer, S. Cherevko, B. Gault, R. van de Krol, C. Scheu, Different Photostability of BiVO4 in Near-pH-Neutral Electrolytes, ACS Appl. Energy Mater. 3 (10) (2020) 9523–9527.
[53] X. Yao, X. Zhao, J. Hu, H. Xie, D. Wang, X. Cao, Z. Zhang, Y. Huang, Z. Chen, T. Sritharan, The Self-Passivation Mechanism in Degradation of BiVO4 Photoanode, iScience 19 (2019) 976–985.
[54] T.W. Kim, K.-S. Choi, Nanoporous BiVO4 Photoanodes with Dual-Layer Oxygen Evolution Catalysts for Solar Water Splitting, Science 343 (6174) (2014) 990.
[55] L. Xia, J. Bai, J. Li, Q. Zeng, L. Li, B. Zhou, High-performance BiVO4 photoanodes cocatalyzed with an ultrathin α-Fe2O3 layer for photoelectrochemical application, Appl. Catal. B 204 (2017) 127–133.
[56] T. Palaniselvam, L. Shi, G. Mettela, D.H. Anjum, R. Li, K.P. Katuri, P.E. Saikaly, P. Wang, Vastly Enhanced BiVO4 Photocatalytic OER Performance by NiCoO2 as Cocatalyst, Adv. Mater. Interf. 4 (19) (2017) 1700540.
[57] F.M. Pesci, G. Wang, D.R. Klug, Y. Li, A.J. Cowan, Efficient Suppression of Electron-Hole Recombination in Oxygen-Deficient Hydrogen-Treated TiO2 Nanowires for Photoelectrochemical Water Splitting, J. Phys. Chem. C 117 (48) (2013) 25837–25844.
[58] C. Martín, M. Ziółek, A. Douhal, Ultrafast and fast charge separation processes in real dye-sensitized solar cells, J. Photochem. Photobiol., C 26 (2016) 1–30.
[59] C. Liu, J. Zhou, J. Su, L. Guo, Turning the unwanted surface bismuth enrichment to favourable BiVO4/BiOCl heterojunction for enhanced photoelectrochemical performance, Appl. Catal. B 241 (2019) 506–513.
[60] M. Zhang, R.P. Antony, S.Y. Chiam, F.F. Abdi, L.H. Wong, Understanding the Roles of NiOx in Enhancing the Photoelectrochemical Performance of BiVO4 Photoanodes for Solar Water Splitting, Chem Sus Chem 12 (9) (2019) 2022–2028.
[61] D.K. Zhong, S. Choi, D.R. Gamelin, Near-Complete Suppression of Surface Recombination in Solar Photoelectrolysis by "Co-Pi" Catalyst-Modified W: BiVO4, J. Am. Chem. Soc. 133 (45) (2011) 18370–18377.
[62] J.A. Seabold, K.-S. Choi, Efficient and Stable Photo-Oxidation of Water by a Bismuth Vanadate Photoanode Coupled with an Iron Oxyhydroxide Oxygen Evolution Catalyst, J. Am. Chem. Soc. 134 (4) (2012) 2186–2192.
[63] F.F. Abdi, L. Han, A.H.M. Smets, M. Zeman, B. Dam, R. van de Krol, Efficient solar water splitting by enhanced charge separation in a bismuth vanadate-silicon tandem photoelectrode, Nat. Commun. 4 (1) (2013) 2195.
[64] F.F. Abdi, D.E. Starr, I.Y. Ahmet, R. van de Krol, Photocurrent Enhancement by Spontaneous Formation of a p–n Junction in Calcium-Doped Bismuth Vanadate Photoelectrodes, Chem Plus Chem 83 (10) (2018) 941–946.
[65] H. Dotan, K. Sivula, M. Grätzel, A. Rothschild, S.C. Warren, Probing the photoelectrochemical properties of hematite (α-Fe2O3) electrodes using hydrogen peroxide as a hole scavenger, Energy Environ. Sci. 4 (3) (2011) 958–964.
[66] B. Xu, P. He, H. Liu, P. Wang, G. Zhou, X. Wang, A 1D/2D Helical CdS/ZnIn2S4 Nano-Heterostructure, Angew. Chem. Int. Ed. 53 (9) (2014) 2339–2343.
[67] G. Wang, H. Wang, Y. Ling, Y. Tang, X. Yang, R.C. Fitzmorris, C. Wang, J.Z. Zhang, Y. Li, Hydrogen-Treated TiO2 Nanowire Arrays for Photoelectrochemical Water Splitting, Nano Lett. 11 (7) (2011) 3026–3033.
[68] M. Ma, K. Zhang, P. Li, M.S. Jung, M.J. Jeong, J.H. Park, Dual Oxygen and Tungsten Vacancies on a WO3 Photoanode for Enhanced Water Oxidation, Angew. Chem. Int. Ed. 55 (39) (2016) 11819–11823.
[69] J.E.B. Randles, Kinetics of rapid electrode reactions, Discuss. Faraday Soc. 1 (1947) 11–19.
[70] S. Wang, T. He, J.-H. Yun, Y. Hu, M. Xiao, A. Du, L. Wang, New Iron-Cobalt Oxide Catalysts Promoting BiVO4 Films for Photoelectrochemical Water Splitting, Adv. Funct. Mater. 28 (34) (2018) 1802685.
[71] B. Klahr, S. Gimenez, F. Fabregat-Santiago, T. Hamann, J. Bisquert, Water Oxidation at Hematite Photoelectrodes: The Role of Surface States, J. Am. Chem. Soc. 134 (9) (2012) 4294–4302.
[72] F.S. Hegner, I. Herraiz-Cardona, D. Cardenas-Morcoso, N. López, J.-R. Galán-Mascarós, S. Gimenez, Cobalt Hexacyanoferrate on BiVO4 Photoanodes for Robust Water Splitting, ACS Appl. Mater. Interfaces 9 (43) (2017) 37671–37681.
[73] B.J. Trześniewski, I.A. Digdaya, T. Nagaki, S. Ravishankar, I. Herraiz-Cardona, D.A. Vermaas, A. Longo, S. Gimenez, W.A. Smith, Near-complete suppression of surface losses and total internal quantum efficiency in BiVO4 photoanodes, Energy Environ. Sci. 10 (6) (2017) 1517–1529.
[74] M. Zhong, T. Hisatomi, Y. Kuang, J. Zhao, M. Liu, A. Iwase, Q. Jia, H. Nishiyama, T. Minegishi, M. Nakabayashi, N. Shibata, R. Niishiro, C. Katayama, H. Shibano, M. Katayama, A. Kudo, T. Yamada, K. Domen, Surface Modification of CoOx Loaded BiVO4 Photoanodes with Ultrathin p-Type NiO Layers for Improved Solar Water Oxidation, J. Am. Chem. Soc. 137 (15) (2015) 5053–5060.
[75] J. Eichhorn, C. Kastl, A.M. Schwartzberg, I.D. Sharp, F.M. Toma, Disentangling the Role of Surface Chemical Interactions on Interfacial Charge Transport at BiVO4 Photoanodes, ACS Appl. Mater. Interfaces 10 (41) (2018) 35129–35136.
[76] N. Guijarro, M.S. Prévot, K. Sivula, Surface modification of semiconductor photoelectrodes, PCCP 17 (24) (2015) 15655–15674.
[77] S.-S. Yi, B.-R. Wulan, J.-M. Yan, Q. Jiang, Highly Efficient Photoelectrochemical Water Splitting: Surface Modification of Cobalt-Phosphate-Loaded Co3O4/Fe2O3 p–n Heterojunction Nanorod Arrays, Adv. Funct. Mater. 29 (11) (2019) 1801902.
[78] J. Bisquert, A. Zaban, M. Greenshtein, I. Mora-Seró, Determination of Rate Constants for Charge Transfer and the Distribution of Semiconductor and Electrolyte Electronic Energy Levels in Dye-Sensitized Solar Cells by Open-Circuit Photovoltage Decay Method, J. Am. Chem. Soc. 126 (41) (2004) 13550–13559.
[79] B.H. Meekins, P.V. Kamat, Got TiO2 Nanotubes? Lithium Ion intercalation can boost their Photoelectrochemical Performance, ACS Nano 3 (11) (2009) 3437–3446.
[80] R.P. Antony, P.S. Bassi, F.F. Abdi, S.Y. Chiam, Y. Ren, J. Barber, J.S.C. Loo, L.H. Wong, Electrospun Mo-BiVO4 for Efficient Photoelectrochemical Water Oxidation: Direct Evidence of Improved Hole Diffusion Length and Charge separation, Electrochim. Acta 211 (2016) 173–182.
[81] O. Goscinski, Principles of Ultraviolet Photoelectron Spectroscopy. J. W. Rabalais. Wiley-Interscience Monographs in Chemical Physics, New York, 1977. Price: $22.50, Int. J. Quantum Chem. 13(2) (1978) 263–263.
[82] B. Cui, H. Lin, X. Zhao, J.-B. Li, W.-D. Li, Visible Light Induced Photocatalytic Activity of ZnCo2O4 Nanoparticles, Acta Phys. Chim. Sin. 27 (2011).

[83] P.G. Radaelli, Orbital ordering in transition-metal spinels, New J. Phys. 7 (2005) 53.
[84] B. Cui, H. Lin, Y.-Z. Liu, J.-B. Li, P. Sun, X.-C. Zhao, C.-J. Liu, Photophysical and Photocatalytic Properties of Core-Ring Structured NiCo2O4 Nanoplatelets, J. Phys. Chem. C 113 (32) (2009) 14083–14087.
[85] A. Sarkar, K. Karmakar, G.G. Khan, Designing Co-Pi Modified One-Dimensional n–p TiO2/ZnCo2O4 Nanoheterostructure Photoanode with Reduced Electron-Hole Pair Recombination and Excellent Photoconversion Efficiency (>3%), J. Phys. Chem. C 121 (46) (2017) 25705–25717.
[86] R. Marschall, Semiconductor Composites: Strategies for Enhancing Charge Carrier Separation to Improve Photocatalytic Activity, Adv. Funct. Mater. 24 (17) (2014) 2421–2440.
[87] The absolute electrode potential, an explanatory note (Recommendations 1986), J. Electroanal. Chem. Interfacial Electrochem. 209 (2) (1986) 417–428.
[88] J. Resasco, H. Zhang, N. Kornienko, N. Becknell, H. Lee, J. Guo, A.L. Briseno, P. Yang, TiO2/BiVO4 Nanowire Heterostructure Photoanodes Based on Type II Band Alignment, ACS Cent. Sci. 2 (2) (2016) 80–88.
[89] C.G. Morales-Guio, S.D. Tilley, H. Vrubel, M. Grätzel, X. Hu, Hydrogen evolution from a copper(I) oxide photocathode coated with an amorphous molybdenum sulphide catalyst, Nat. Commun. 5 (1) (2014) 3059.
[90] A. Song, S.P. Berglund, A. Chemseddine, D. Friedrich, F.F. Abdi, R. van de Krol, Elucidating the optical, electronic, and photoelectrochemical properties of p-type copper vanadate (p-Cu5V2O10) photocathodes, J. Mater. Chem. A 8 (25) (2020) 12538–12547.
[91] S.N.S.B.H. Yassin, A.S.L. Sim, J.R. Jennings, Photoelectrochemical evaluation of SILAR-deposited nanoporous BiVO4 photoanodes for solar-driven water splitting, Nano Mater. Sci. 2 (2020) 227–234.
[92] X. Li, J. Wan, Y. Ma, Y. Wang, X. Li, Study on cobalt-phosphate (Co-Pi) modified BiVO4/Cu2O photoanode to significantly inhibit photochemical corrosion and improve the photoelectrochemical performance, Chem. Eng. J. 404 (2021) 127054.
[93] M.A. Butler, Photoelectrolysis and physical properties of the semiconducting electrode WO2, J. Appl. Phys. 48 (5) (1977) 1914–1920.
[94] P. Dias, L. Andrade, A. Mendes, Hematite-based photoelectrode for solar water splitting with very high photovoltage, Nano Energy 38 (2017) 218–231.
[95] C. Du, X. Yang, M.T. Mayer, H. Hoyt, J. Xie, G. McMahon, G. Bischoping, D. Wang, Hematite-Based Water Splitting with Low Turn-On Voltages, Angew. Chem. Int. Ed. 52 (48) (2013) 12692–12695.
[96] Y. Hermans, S. Murcia-López, A. Klein, R. van de Krol, T. Andreu, J.R. Morante, T. Toupance, W. Jaegermann, Analysis of the interfacial characteristics of BiVO4/metal oxide heterostructures and its implication on their junction properties, PCCP 21 (9) (2019) 5086–5096.
[97] X. Yin, W. Qiu, W. Li, C. Li, K. Wang, X. Yang, L. Du, Y. Liu, J. Li, High porosity Mo doped BiVO4 film by vanadium re-substitution for efficient photoelectrochemical water splitting, Chem. Eng. J. 389 (2020) 124365.
[98] R. Liu, Z. Zheng, J. Spurgeon, X. Yang, Enhanced photoelectrochemical water-splitting performance of semiconductors by surface passivation layers, Energy Environ. Sci. 7 (8) (2014) 2504–2517.
[99] A. Ghobadi, T.G.U. Ghobadi, F. Karadas, E. Ozbay, Angstrom Thick ZnO Passivation Layer to Improve the Photoelectrochemical Water Splitting Performance of a TiO2 Nanowire Photoanode: The Role of Deposition Temperature, Sci. Rep. 8 (1) (2018) 16322.
[100] X. Cheng, S. Cao, Y. Huan, Z. Bai, M. Li, H. Wu, R. Zhang, W. Peng, Z. Ji, X. Yan, The Synergetic Benefits of Passivation Layer and Catalytic Layer on Hematite for Efficient Water Splitting, Energy Technol. 7 (4) (2019) 1800899.
[101] L. Meng, W. Tian, F. Wu, F. Cao, L. Li, TiO2 ALD decorated CuO/BiVO4 p-n heterojunction for improved photoelectrochemical water splitting, J. Mater. Sci. Technol. 35 (8) (2019) 1740–1746.